2010

Angular variation of absorption and thermal emission enhancement from the two dimensional photonic crystals

Weijun Zhao
Iowa State University

Angular variation of absorption and thermal emission enhancement from the two dimensional photonic crystals

by

Weijun Zhao

A thesis submitted to the graduate faculty

in partial fulfillment of the requirements for the degree of

MASTER OF SCIENCE

Major: Electrical Engineering

Program of Study Committee:

Rana Biswas, Major Professor

Jaeyoun Kim

Jiming Song

Iowa State University

Ames, Iowa

2010

TABLE OF CONTENTS

LIST OF FIGURES

LIST OF TABLES

ABSTRACT

Photonic crystal structures and their applications are an active growing research area in the scientific community. The photonic crystals can have a complete bandgap for proper choice of the structure and dielectric contrast. Photonic crystal structures are very useful in many areas such as photovoltaic devices, infrared sources and optic fibers.

The photonic crystal structures have been used in the thermal photovoltaic devices and as a narrow band infrared emitter. In this thesis we investigate the angular variation of absorption and thermal emission from the two-dimensional metallic and metal-dielectric photonic crystal structures by using rigorous scattering matrix method. We found that the thermal emission of these photonic crystals at different wavelengths is redistributed into different emission angles. The photon emission are partially suppressed at long wavelengths and enhanced at the shorter wavelength range. We utilized the surface plasmon models to describe the angular dependent absorption. The strong spectral variation of the thermal emission with angle should be accounted for the thermo-photovoltaic devices utilizing photonic crystals.

We also propose a metallic photonic crystal for incandescent filaments. We simulated the tungsten photonic crystals and found that by using the photonic crystals it is possible to increase the lifetime and brightness of light bulbs. We also present results for metal-dielectric patches at infrared length scales and find absorption peaks can be tuned by the geometry of the patch.

CHAPTER 1 INTRODUCTION

2D Photonic Crystals

We use extensively the two dimensional (2D) photonic crystals. Here we summarize the basic properties of 2D photonic crystals. 2D photonic crystals are artificial structures with periodic dielectric constants in two dimensions and can exhibit photonic band gaps, in which electromagnetic waves in a certain wavelength range can not propagate in the plane of the structure. Due to the ease of fabrication compared to 3D photonic crystals, the 2D photonic crystals have attracted a great deal of attention in recent years. Figure 1.1 shows the 2D photonic crystal structures with both square and triangular lattice of holes going through a slab.

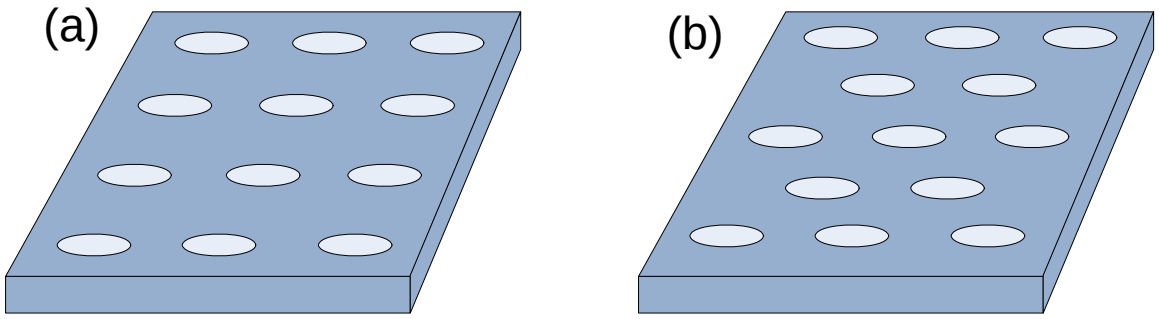

Figure 1.1 (a) 2D photonic crystal structure with square lattice of holes in a dielectric slab.
(b) 2D photonic crystal structure with triangular lattice of holes in a dielectric slab.

Diffracting Structures

In this thesis we consider incident waves normal to the 2D photonic crystal and in general out of the plane of the structure at an angle to the normal direction, in contrast to the propagation in the plane of the structure. For this situation of waves incident from out of the

plane of the structure, the 2D photonic crystals are diffracting grating structures due to the periodic arrangement of the holes or cylinders in a substrate. Figure 1.2 shows both the incident and reflected field components. The wave vector and electric field vector of the incident field could be described as,

$$k_i = k_{ix}\hat{x} + k_{iy}\hat{y} + k_{iz}\hat{z} \tag{1.1}$$

$$\boldsymbol{E_i} = \boldsymbol{E_0}\, e^{(-j\,\mathbf{k_i r})} = \boldsymbol{E}_0\, e^{(-j(k_x x + k_y y + k_z z))} \tag{1.2}$$

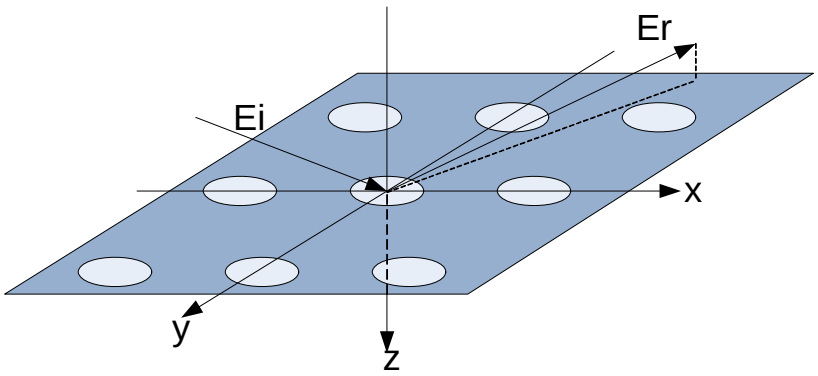

Figure 1.2 The schematic of the incident wave and reflected wave the 2D square lattice of the photonic crystal structure.

Using the Rayleigh expansions [1, 2] the reflected field vector could be expressed as,

$$\boldsymbol{E_r} = \sum_{m,n} B_{mn} e^{(-j\,\mathbf{k}_{r,mn}\,\mathbf{r})} \tag{1.3}$$

where the integers *m* and *n* are defined as the order of the diffracted waves and the B_{mn} is the magnitude of the (m, n) order diffracted wave.

According to the phase matching condition and the Floquet condition, the wave vector of the reflected field is,

$$k_{r,mn} = k_{xm}\hat{x} + k_{yn}\hat{y} + k_{zr,mn}\hat{z} \tag{1.4}$$

where the k_{xm}, k_{yn} and $k_{zr,mn}$ are expressed as,

$$\begin{aligned} k_{xm} &= k_x + mG_x \\ k_{yn} &= k_y + nG_y \\ k^2_{zr,mn} &= k_i^2 - k_{xm}^2 - k_{yn}^2 \end{aligned} \tag{1.5}$$

where the G_x and G_y define the unit vectors of the reciprocal lattice vector G. The G_x and G_y are inversely proportional to the lattice constant a of the 2D photonic crystal and for the square lattice in shown Figure 1.2 they can be expressed as,

$$G_x = G_y = 2\pi/a \tag{1.6}$$

If $k^2_{zr,mn}$ is larger than zero, then the reflected wave is a propagating wave. Or else the reflected wave is an evanescent wave with exponentially decaying field magnitude away from the lattice interface if $k^2_{zr,mn}$ is less than zero.

Subwavelength Hole Array

In 1998, T. W. Ebbesen et al. discovered the extraordinary optical transmission through the sub-wavelength holes array in a thin film metal [3]. They fabricated a two dimensional arrays of cylindrical cavities in a thin (0.2 μm) layer metal film which sits above the quartz substrate. Several distinct features were found in the measured zero-order transmission spectrum of the structure [Figure 1.3 (a)].

The holes array structures fabricated by T. W. Ebbesen et al. are in subwavelegnth regime. The waveguide modes in a single cylindrical cavity only exist above certain cutoff frequency [Figure 1.4]. The first order waveguide mode TE11 is formed in the holes at the cutoff wavelength $\lambda=3.42R$, which is smaller than the period of the hole array. Thus there are no waveguide modes formed in the holes above the wavelength corresponding to the period of the hole array.

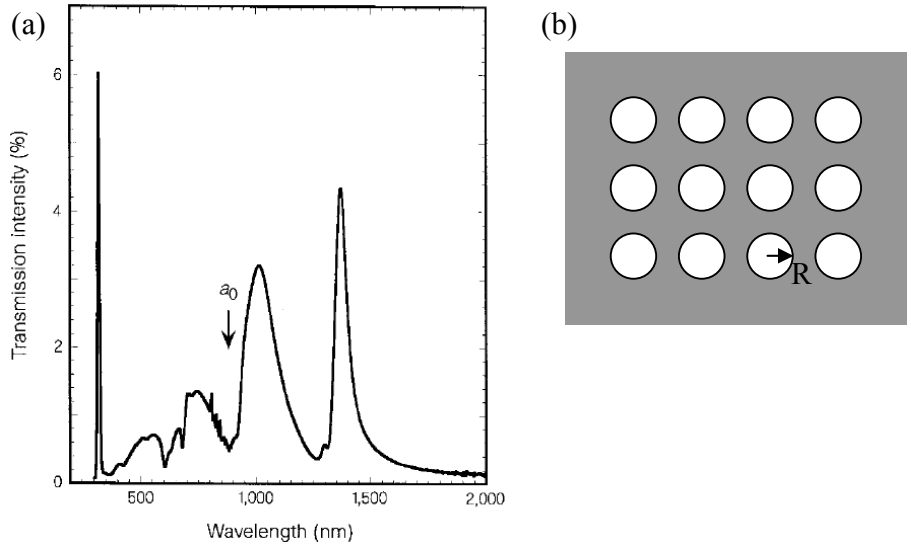

Figure 1.3 (a) Zero-order transmission spectrum of a subwavelength holes array in a metallic film with period of 0.9 μm and metal layer thickness of 200 nm [3]. (b) Top view of the holes array. R is the radius of the hole.

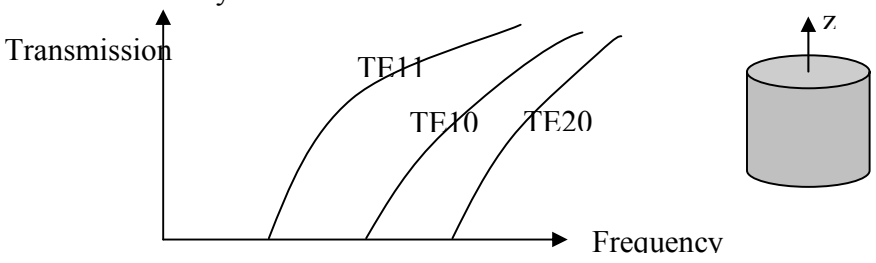

Figure 1.4 The first three orders of TE waveguide modes in a circular cavity

Figure 1.3 (a) shows is a distinctive transmission minimum near the wavelength corresponding to the pitch size of the holes array, which could be explained by the Wood's anomaly, where the diffracted order changes from evanescent to propagating wave,

$$\lambda_{n,m} = \frac{a}{\sqrt{n^2 + m^2}} \tag{1.7}$$

The wavelength from the first Wood's anomaly (m or n is zero) is at a, which is the period of the hole array.

There is one remarkable transmission peak when the wavelength is slightly larger than a, which is caused by the excitation of surface plasmons at the metal interface when the momentum of the surface plasmons that match the momentum of the incident photons and the grating,

$$k_{sp} = k_x \pm nG_x \pm mG_y \tag{1.8}$$

where the *Gx* and *Gy* have the same definition as in equation 1.6. The other transmission peak near the wavelength that corresponds to a·n (n is the refractive index of quartz) is the surface plasmons at the metal-quartz interface.

L. Martín-Moreno et al. later fabricated the two dimensional hole arrays in a thin free-standing metal film [8]. The zero-order transmission of the freestanding thin film is measured [Figure 1.5]. A strong transmission peak at the wavelength slightly larger than the period of the hole arrays was observed, which would not expected by the classical waveguide modes since the hole arrays are in sub-wavelength regime. One difference from the metal film onthe quartz substrate in [3] is that the freestanding metal film has the same metal-dielectric (air)

interface on the two sides. Surface plasmons are excited at both metal-dielectric interfaces of the freestanding metal film. The surface plasmons at the two interfaces are strongly coupled, which leads to the extraordinary transmission of light near the wavelength slightly above the period of hole arrays. The enhancement factor, which is the ratio of the transmitted intensity to the incident intensity normalized to the area of the holes, can exceed a factor of 5.

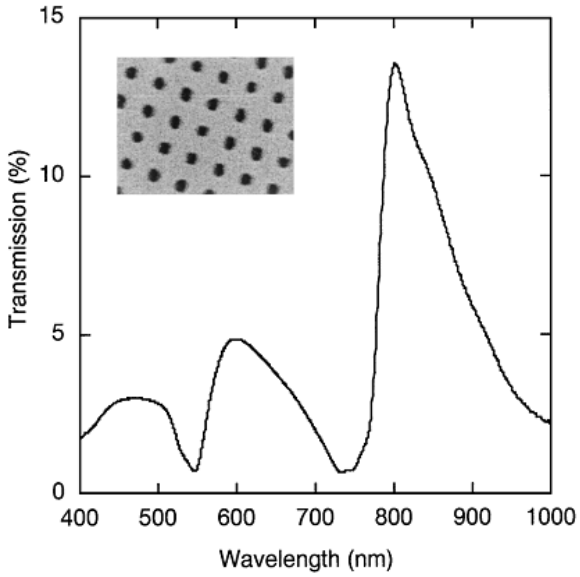

Figure 1.5 Experimental zero-order power transmittance at normal direction for a square array of holes (period 750nm) in a freestanding Ag film (thickness 320nm). Inset shows the SEM of the perforated metal film [8].

Scattering Matrix Method

The main simulation method used in the thesis is the rigorous Scattering Matrix Method. The Scattering Matrix Method is based on the well-known Transfer Matrix Method (TMM) [9, 5]. The Scattering Matrix Method can be used to calculate the transmission and reflection from layer by layer structures [Fig 1.2]. The slab material in z direction is homogeneous. In each layer a scattering matrix is defined,

$$\begin{pmatrix} \Omega_i^+ \\ \Omega_{i-1}^- \end{pmatrix} = \begin{pmatrix} s^i \end{pmatrix} \begin{pmatrix} \Omega_{i-1}^+ \\ \Omega_i^- \end{pmatrix} \tag{1.9}$$

in which the Ω_i^+ and Ω_i^- are the Fourier components of electric fields in forward and reverse directions respectively in the i_{th} layer. Then the total S matrix can be obtained by the standard recursion relation through all the layers in the entire structure.

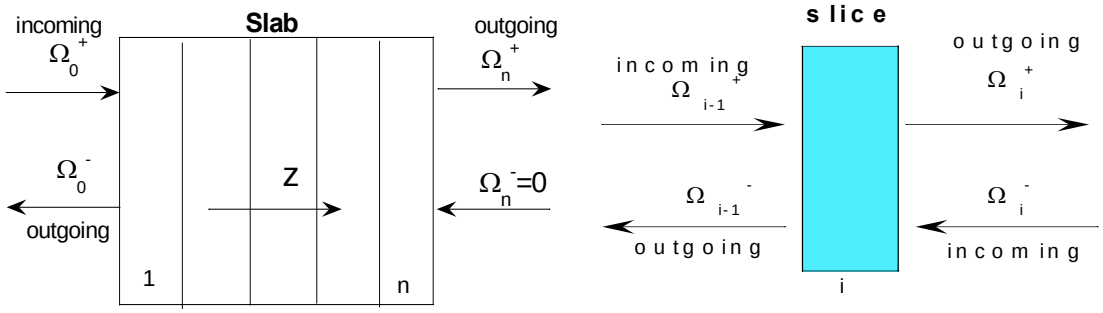

Figure 1.6 (a) definition of S matrix for photonic crystal structure with n layers. (b) definition of S matrix for an individual layer.

To calculate the S matrix for each layer the continuity condition of E and H fields at each interface is used. The dielectric constant ε in each individual layer only varies with x and y. The Fourier transform of the ε and ε^{-1} is,

$$\begin{aligned} \varepsilon(r) &= \sum_{ij} \varepsilon_{ij} e^{(-jG_{ij}r)} \\ \varepsilon^{-1}(r) &= \sum_{ij} \varepsilon^{-1}{}_{ij} e^{(-jG_{ij}r)} \end{aligned} \tag{1.10}$$

where $\boldsymbol{r}=x\,\hat{x}+y\,\hat{y}$. The z dependence of the in-plane electric fields can be obtained by decomposing the time harmonic Maxwell Equation,

$$\begin{aligned} \nabla \times E(r) - j\omega\mu H(r) = 0 \\ \nabla \times H(r) + j\omega\varepsilon(r)E(r) = 0 \end{aligned} \tag{1.11}$$

which leads to,

$$\begin{aligned} \frac{\partial}{\partial z}E_x &= \frac{1}{jk_0}\frac{\partial}{\partial x}[\frac{1}{\varepsilon(x,y)}(\frac{\partial}{\partial x}H_y - \frac{\partial}{\partial y}H_x)] - jk_0H_y \\ \frac{\partial}{\partial z}E_y &= \frac{1}{jk_0}\frac{\partial}{\partial y}[\frac{1}{\varepsilon(x,y)}(\frac{\partial}{\partial y}H_x - \frac{\partial}{\partial x}H_y)] + jk_0H_x \end{aligned} \tag{1.12}$$

Substitute ε^{-1} in equation 1.10 into 1.12 and rewrite the fields in the forms of equation 1.3, we obtain,

$$\begin{aligned} \frac{\partial}{\partial z}E_{ij,x} &= \frac{jk_{ij,x}}{k_0}\sum_{mn}\varepsilon^{-1}{}_{ij,mn}(k_{mn,x}H_{mn,y} - k_{mn,y}H_{mn,x}) - jk_0H_{ij,y} \\ \frac{\partial}{\partial z}E_{ij,y} &= \frac{jk_{ij,y}}{k_0}\sum_{mn}\varepsilon^{-1}{}_{ij,mn}(k_{mn,x}H_{mn,y} - k_{mn,y}H_{mn,x}) - jk_0H_{ij,x} \end{aligned} \tag{1.12}$$

The other two equations for the H fields can be derived through the same procedures. The equation 1.7 can be rewritten in a matrix form with column vectors $E=(..., E_{ij,x}, E_{ij,y}, ...)^T$ and $H=(..., H_{ij,x}, H_{ij,y}, ...)^T$,

$$\frac{\partial}{\partial z}E = M_1H \tag{1.13}$$

And similarly,

$$\frac{\partial}{\partial z}H = M_2E \tag{1.14}$$

Combining equations 1.13 and 1.14 we get,

$$\frac{\partial^2}{\partial z^2} E = M_1 M_2 E \tag{1.15}$$

which is an eigen-value problem and can be solved for each layer using the fields continuity boundary conditions at each interface. The total S matrix for the entire layered structure then can be obtained by applying the standard recursion relations to the scattering matrices (S_i) in each layer. The reflection and transmission of the layered structure then can be calculated from the total S matrix.

One of the advantages of the Scattering Matrix Method is that the parallel computational algorithm can be easily realized with each frequency sent to an individual processor since the scattering matrix simulation is performed in frequency domain. The final frequency response of the structure can be found by concatenating the results at different frequencies.

Research Motivation

The 2D photonic crystal structures have found many applications in diverse areas. Due to the diffracting effect in the photonic crystals, their reflection, transmission and absorption have strong angular dependence. In the recent research work of applying photonic crystals in the solar cells to increase the efficiency, the emission from photonic crystals is considered only in a small angle near the normal direction [10]. In this thesis we study the angular dependence of the emission characteristic of the 2D photonic crystal in all the angles, from 0° to 70°. Furthermore, the metallic 2D photonic crystals are proposed to enhance the thermal emission of incandescent sources. We mainly focus on the 2D metallodielectric and metallic photonic crystal structures [Figure 1. 6]. In both the metallodielectric and metallic

photonic crystals the two dimensional hole arrays are sitting above a optically thick substrate, which results in zero transmission and converted the extraordinary transmission in a thin metal film into the enhanced absorption at the wavelength near the period of the hole arrays. In the metallic photonic crystal there is no transmission and the signature of the resonance is a strong reflection minimum accompanied by an absorption maximum.

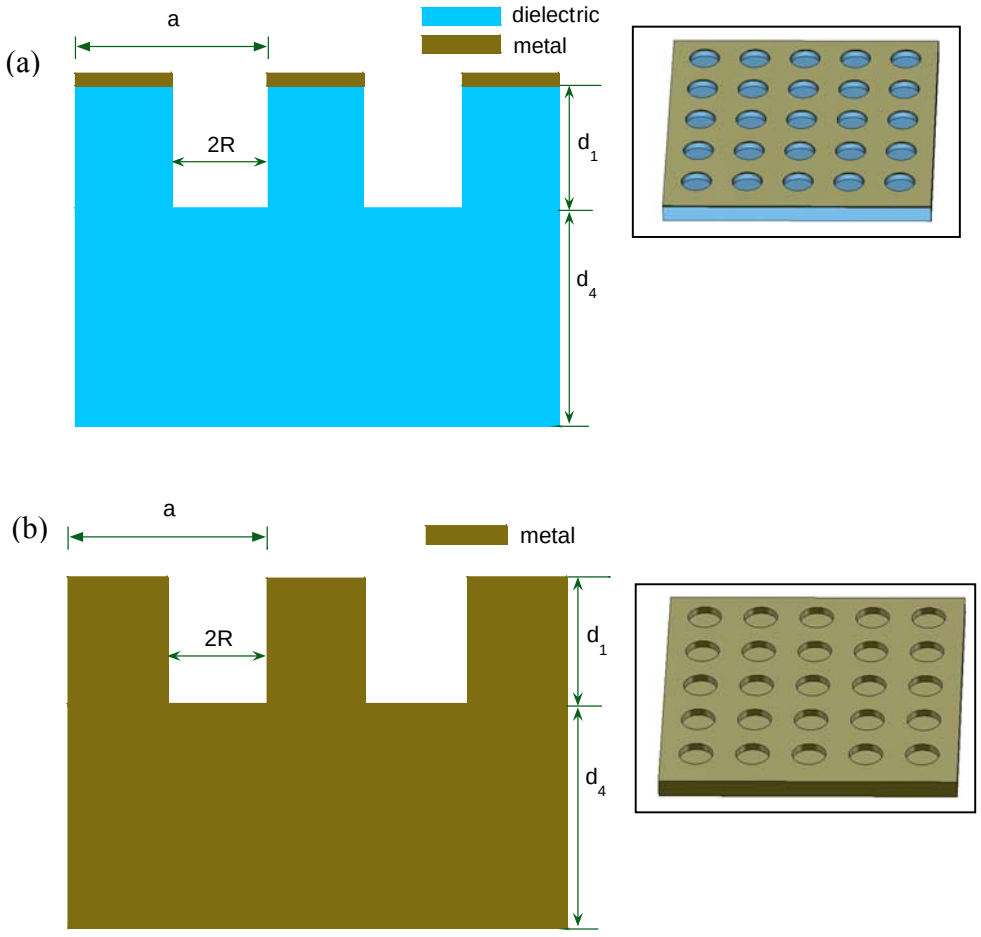

Figure 1.7 (a) Schematic of the 2D metallodiectric photonic crystal. (b) Schematic of the 2D metallic photonic crystal. Both the insets shows the viewgraphs of the photonic crystals.

Organization of the thesis

The rest part of the thesis is organized as follows. Chapter 2 investigates the angular distribution of absorption and thermal emission in both 2D metallic and metallo-dielectric photonic crystals. Chapter 3 discusses the enhancement of thermal emission by utilizing the 2D tungsten photonic crystals.

In Chapter 4, periodic arrays of microstrip patches are discussed. The microstrip patch arrays can exhibit broadband infrared absorption near IR wavelength if properly designed. This chapter serves as suggestions for future work.

References

1. R. Petit, Electromagnetic Theory of Gratings (Springer-Verlag, Berlin, 1980).
2. S. Peng and G. M. Morris, J. Opt. Soc. Am. A. 13, 993 (1996).
3. T. W. Ebbesen, H. J. Lezec, H. F. Ghaemi, T. Thio, and P. A.Wolff, "Extraordinary optical transmission through subwavelength hole arrays," Nature **391**, 667-669 (1998).
4. I. Puscasu, M. Pralle, M. McNeal, J. Daly, A. Greenwald, E. Johnson, R. Biswas and C. G. Ding, "Extraordinary emission from two dimensional plasmonic-photonic crystals", J. Appl. Phys. **98**, 13531 (2005).
5. R. Biswas, C.G. Ding, I. Puscasu, M. Pralle, M. McNeal, J. Daly, A. Greenwald, E. Johnson, "Theory of subwavelength hole arrays coupled with photonic crystals for extraordinary thermal emission" , Phys. Rev. B. **74**, 045107 (2006).

6. R. Biswas, S. Neginhal, C. G. Ding, I. Puscasu, E. Johnson, "Mechanisms underlying extraordinary transmission in sub-wavelength hole arrays", J. Opt. Soc. of America B 24, 2489-2596 (2007).

7. R. Biswas, D. Zhou, I. Puscasu, E. Johnson, A. Taylor and W. Zhao, "Sharp thermal emission and absorption from conformally coated metallic photonic crystal with triangular lattice" , Appl. Phys Lett. **93**, 063307 (2008).

8. L. Martin-Moreno, F. J. Garcia-Vidal, H. J. Lezec, K. M.Pellerin, T. Thio, J. B. Pendry, and T. W. Ebbesen, "Theory of extraordinary optical transmission through subwavelength hole arrays," Phys. Rev. Lett. 86, 1114-1117 (2001).

9. Z. Y. Li and L. L. Lin, "Photonic band structures solved by a plane-wave-based transfer-matrix method", Phys. Rev. E **67**, 046607 (2003).

10. M. Florescu, H. Lee, I. Puscasu, M. Pralle, L. Florescu, D. Z. Ting, J. P. Dowling, "Improving solar cell efficiency using photonic band-gap materials", Solar E**ne**rgy Materials and Solar Cells **91**, 1599-1610 (2007).

CHAPTER 2 ANGULAR VARIATION OF ABSORPTION AND THERMAL EMISSION FROM PHOTONIC CRYSTALS

A paper published in J. Opt. Soc. Am. B., **26**, 1808-1817 (2009)

W. Zhao[1], R. Biswas[1,2,*], I. Puscasu[3], E. Johnson[3]

[1] Microelectronics Research Center and Dept. of Electrical and Computer Engineering, Iowa State University, Ames, IA 50011.

[2] Department of Physics and Astronomy, Ames Laboratory, Iowa State University, Ames, IA 50011

[3] ICX-Photonics, Billerica, MA 01821

Abstract

The absorption and thermal exitance of two dimensional metallic and metallodielectric photonic crystals is simulated with rigorous scattering matrix methods. These photonic crystals have strong thermal exitance and absorption peaks in the normal direction that shift to larger and smaller wavelengths as the angle varies away from the normal direction. These photonic crystals redistribute the thermal emission at different wavelengths into different emission angles. There is partial suppression of photon emission at long wavelengths and enhancement at the shorter wavelength spectral range where the thermal exitance has a maximum. Surface plasmon models describe well the angular dependent absorption. Thermo-photovoltaic devices utilizing photonic crystals need to account for the strong spectral variation of the thermal exitance with angle.

Introduction

Metallic and metallodielectric photonic crystals (PCs) have attracted much interest in modifying the thermal emission from the black-body [1 - 4] spectrum. These PCs exhibit a sharp absorption feature at a wavelength near the lattice period (a). The thermal exitance of a heated photonic crystal can be considered to be the convolution of the black-body emission with the absorption profile of the PC. Thus, thermal emission of the PC is observed in a narrow band of wavelengths controlled by the absorption profile. Such photonic crystal based selective emitters have diverse applications as infrared sources, infrared sensors, and efficient incandescent sources.

This selective wavelength emission from PCs has attracted much interest in novel thermophotovoltaic (TPV) systems [5 - 7]. PCs could capture solar radiation and be heated to an elevated temperature T. The PC is proposed to emit in a narrow band of wavelengths (centered at frequency ν) which would be captured by a low-band gap absorber, with a band gap E_g, below the peak of the photon energies ($E_g<h\nu$), thus converting solar photons to electrical current. Energy conversion efficiencies have been examined for temperatures T in the range of 1100-1300 K, corresponding to the narrow band gap GaSb solar absorbers of band gap 1.7 eV. Such PCs can also convert waste heat from engines and mechanical processes into useful forms of energy.

We critically examine the fundamental basis of this energy conversion process, especially the wavelength selective emission. Narrow band thermal emission from PCs is observed in a near normal direction, typically in a cone of 10-15º near the normal. A central issue is how the PC emission differs from a black-body of the same temperature (T). It has

been suggested that, in a small cone of angles near the normal direction, the enhanced emission of the PCs at the spectral range is due to the funneling of the thermal emission from the forbidden spectral range of the PC (where the absorption/emission is very low) into the allowed spectral range where there the PC has a large absorption [8]. In one the first studies of three dimensional tungsten PCs [9] with near-optical periods, it was suggested that thermal emission of infrared photons would be suppressed and recycled into the optical region. Much of such previous experiments [9,10,11] and analyses are based on thermal emission in near-normal directions which is easy to measure. However to examine this energy conversion hypothesis it is necessary to determine the emission of the PC into all solid angles - a feature that has not been addressed much in previous work. We perform detailed calculations of the absorption $A(\lambda,\theta,\phi)$ and emission $M(\lambda,T,\theta,\phi)$ of metallic and metallodielectric PCs for off-normal angles. We compare the simulation results with measurements of the metallodielectric PC.

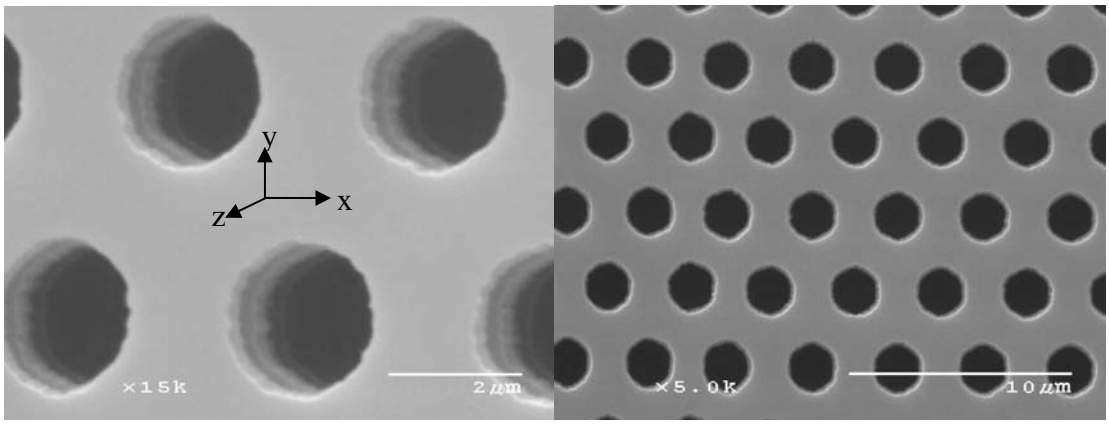

Figure 2.1 Scanning electron microscope images of the metallic PC with triangular lattice.

To study the thermal emission from PCs we utilize a recent metallic PC [Fig 2.1] developed at Iowa State [10] and a metallodielectric PC developed at ICX-Photonics [2,4]. However the results are generally applicable for two dimensional PCs.

Calculation

Simulations were performed with the well-established rigorous scattering matrix method, in which Maxwell's equations are solved for both polarizations in Fourier space and the electric/magnetic fields are expanded in Bloch waves for a periodic PC structure. In the scattering matrix method, the PC with periodicity along x and y directions, is divided into slices along z. The transfer matrix of each layer is diagonalized to obtain the eigen-modes and eigen-frequencies in each layer, thereby leading to a scattering matrix of the individual layer [12]. Through standard recursion relations, scattering matrices of each layer are combined to obtain the scattering matrix for the entire PC structure, from which we simulate the reflection and transmission, and obtain the absorption for each wavelength [4,13]. By varying the incident angle (θ,ϕ) we obtain the angle-dependent absorption profile $A(\lambda,\theta,\phi)$ through computationally intensive simulations. Upto 535 plane waves or a matrix size of 1070 was utilized for achieving convergence in the scattering matrix calculations. The computational algorithm can be easily parallelized since each the solution of Maxwell's equations for each frequency is independent and can be simulated on a separate processor. The simulations were performed on a cluster that has 84 Pentium 4 (3.06 GHz) CPUs at Iowa State University. The simulation requires large memory (~1 GBytes) and long computation time (~1.4 hours/frequency/processor) for each run. We verified that the simulation results converge well with 535 plane waves.

To obtain absorption $A(\lambda,\theta,\phi)$, we simulate the reflection and transmission of the PC for incident angles θ =0-70° and azimuthal angle ϕ=0° and 30° for both s and p polarization. Both specular and non-specular reflection (R_{ns}) and transmission (T_{ns}) are simulated. The transmission is practically zero because the metal substrate is thick (>10μm). From Kirchhoff's Law $A(\lambda,\theta,\phi)+R_{ns}(\lambda,\theta,\phi)+T_{ns}(\lambda,\theta,\phi)=1$, we determine the absorption $A(\lambda,\theta,\phi)=1-R_{ns}(\lambda,\theta,\phi) - T_{ns}(\lambda,\theta,\phi)$. For the PCs, $A(\lambda,\theta)$ is obtained by averaging $A(\lambda,\theta,\phi)$ over s, p polarizations and ϕ=0°, 30° as will be discussed later. Due to the lattice symmetry rotations through azimuthal angles of 60° are equivalent.

According to the Kirchhoff's law, the thermal exitance $M(\lambda,T,\theta)$ is the black body exitance $MBB(\lambda,T)$ modified by the absorption profile $A(\lambda,\theta)$, and can be applied to lossy photonic crystals [14]:

$$M(\lambda,T,\theta)=A(\lambda,\theta)\cdot MBB(\lambda,T). \tag{2.1}$$

$MBB(\lambda,T)$ is the well-known Planck black body exitance,

$$M_{BB}(\lambda,T)=\frac{2\pi hc^2}{\lambda^5\left[e^{hc/\lambda kT}-1\right]} \tag{2.2}$$

λ ,T represent wavelength and temperature, k is the Stefan-Boltzmann constant, h is Planck's constant, and c is the speed of light.

Simulation and Results

We simulate a simple metallic platinum PC absorber consisting of a triangular lattice of holes with radius R, depth d_1 and lattice period a, in a metallic platinum film. Fabrication

of this metallic 2-d PC is substantially easier than the three dimensional woodpile PC [9] and metallo-dielectric PC [4] since only a single layer of periodic structure is needed in this metallic PC. We discuss later the performance trade-offs with our simpler 2-d PC. Platinum is used due to its high melting point (~2045K) and since it is has been employed in high temperature emitting photonic crystal structures [4]. As in previous work [4], the frequency dependent dielectric response of Pt was modeled by the Drude model which is fitted to the measured dielectric functions of bulk Pt (with ν_p=1245 THz and ν_t=16.74 THz), which is a very good representation at infrared wavelengths.

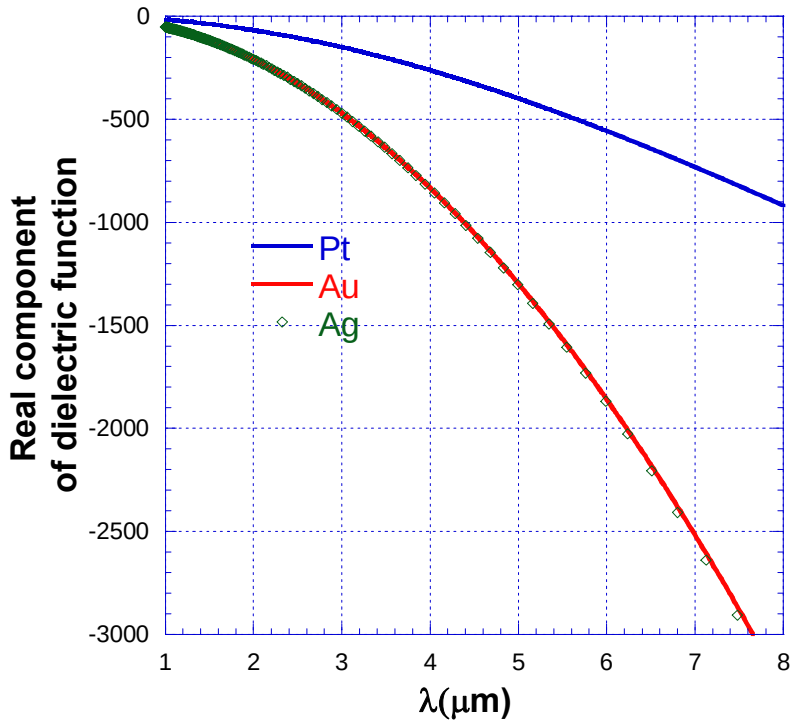

Figure 2.2 Real components of the dielectric function for Pt, Au and Ag in the infrared wavelength range.

The hole radius R is small (R/a=0.25) so that the cut-off wavelength for the fundamental TE(11) propagating mode in a circular waveguide (λ_c=3.42·R) is less than a.

Therefore no classical waveguide modes can transmit through the sub-wavelength holes for incident wavelengths λ near a. The depth of the corrugated metal layer (d_1) is typically larger than a/2. Calculations are shown for a=4 μm, corresponding to wavelengths in the mid infrared band (3 - 6 μm), but results can be scaled to other lattice spacings and wavelengths. The scaling is reasonable as long as real component of the metal dielectric function in PC is negative and large in magnitude, typically in the mid infrared wavelength range [Fig 2.2].

However the scaling breaks down in the optical wavelength range when the real component of the metal dielectric function approaches zero. The real components of dielectric functions for Pt, Au and Ag behave similarly in the mid infrared wavelength [Fig 2.2], although Re(ε) is more negative for Au/Ag than for Pt. Thus the simulated absorption shows a somewhat broader peak for Pt than for Au and Ag [Fig 2.3(a)], since Au/Ag is more similar to an ideal metal than Pt. In experiment, metal is coated conformally on the silicon PC [10]. As long as the thickness of the coated metal is larger than its skin depth (e.g. ~25 nm for Au/Pt at IR wavelength) the structure will behave as a bulk metal with triangular hole lattice. Therefore we use bulk metal values in the Drude model. We focus on Pt for the remainder of the paper.

There is a strong absorption peak at 3.7 μm for normally incident light [Fig 2.3(a)]. As found experimentally the absorption strength is optimized for deep holes with depth d_1>a/2 so that evanescent modes decay within the holes, providing strong absorption at the resonant wavelength [4]. The depth d_1 controls the width of the peak in absorption profile [Fig 2.3(b)]. Shallower holes generate very narrow absorption peaks, which broaden and

become stronger as the depth approaches 2 μm (d_1~a/2) [Fig 2.3b]. When the incident angle is increased to 30°

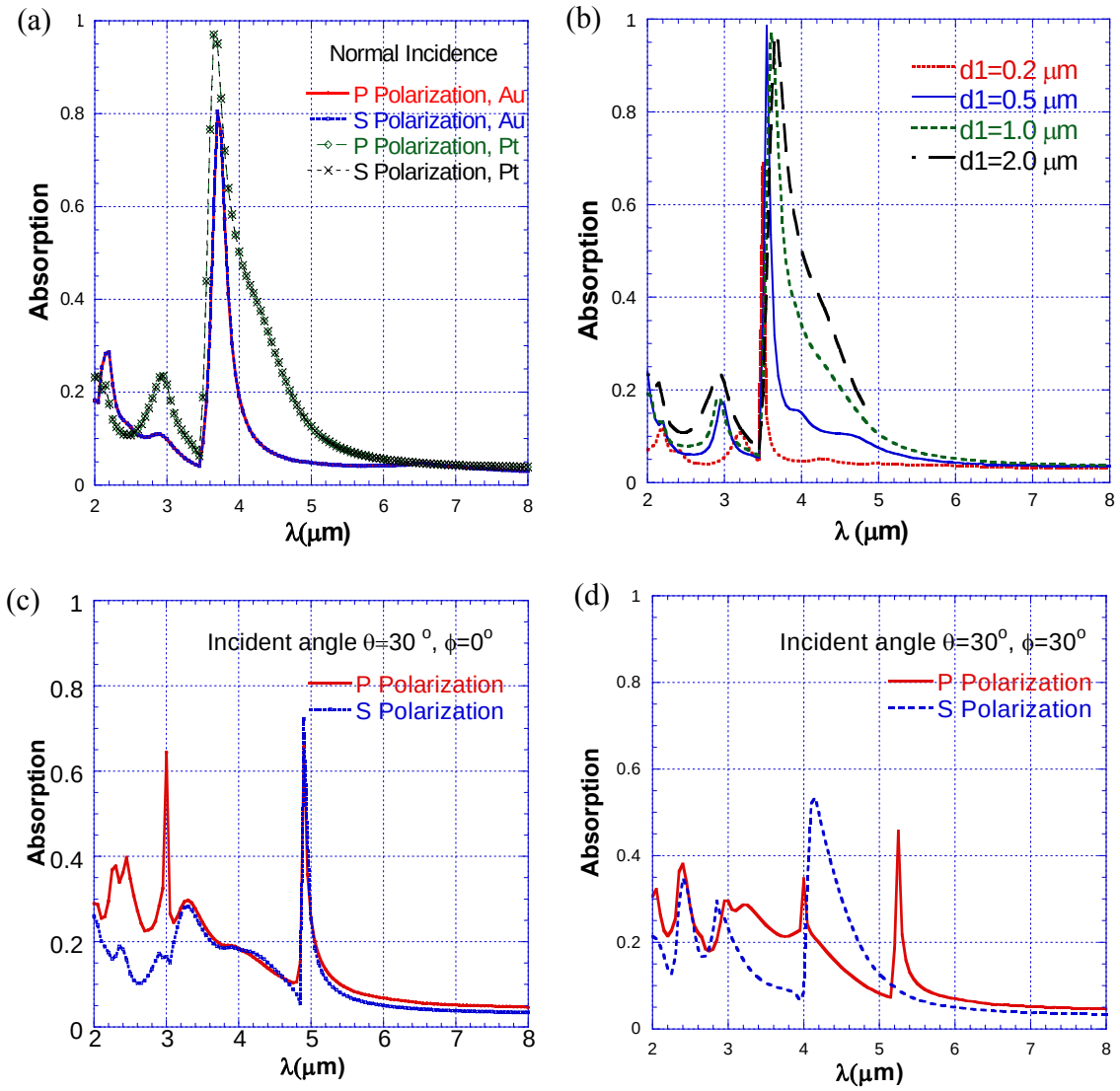

Figure 2.3 (a)Absorption as a function of wavelength for a Pt metallic PC with triangular lattice symmetry. The incident radiation is in the normal direction. Shown for comparison is a simulation for an Au metallic PC with the same parameters as Pt metallic PC. (b) Absorption of the Pt metallic PC with different depths of holes. (c) The incident radiation is at 30º to the normal, the azimuthal angle is 0°. (d) The incident radiation is at 30º to the normal, the azimuthal angle is 30°.

[Fig 2.3 (c) (d)], the s and p polarizations are no longer degenerate. When the azimuthal angle ϕ=0°, the absorption splits into a longer wavelength peak (4.9 μm) for both polarization, and a shorter wavelength peak (3 μm) for p-polarization. Both absorption peaks are weaker than at normal incidence. When the azimuthal angle ϕ=30°, the absorption produces a longer wavelength peak (5.3 μm) for p-polarization. But there are weak absorption peaks staying near 4 μm for both polarizations [Fig 2.3(d)]. The azimuthal angles of 0° and 30° are adequate to represent intermediate values between 0° and 30°. For example, the position of the main absorption peaks changes by less than 16 percent (4%) when the azimuthal angle increases from 0° to 30° for both s-polarization (p-polarization), when the incident angle θ=30° [Fig 2.4].

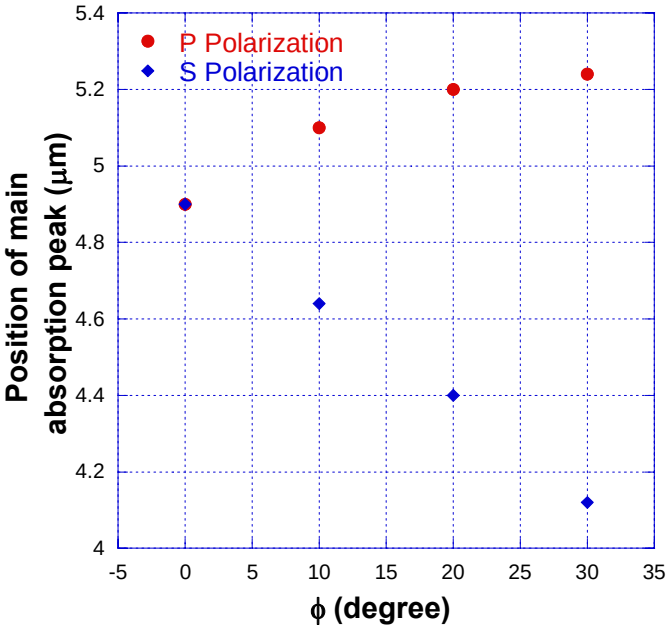

Figure 2.4 Position of main absorption peaks in metallic PC (Pt) with respect to the azimuthal angle for both polarizations when the incident angle is 30°.

Thus using 0° and 30° is a reasonable first approximation to reducing the computational load.

We collected together absorption calculations at all incident angles θ =0-70° in a two

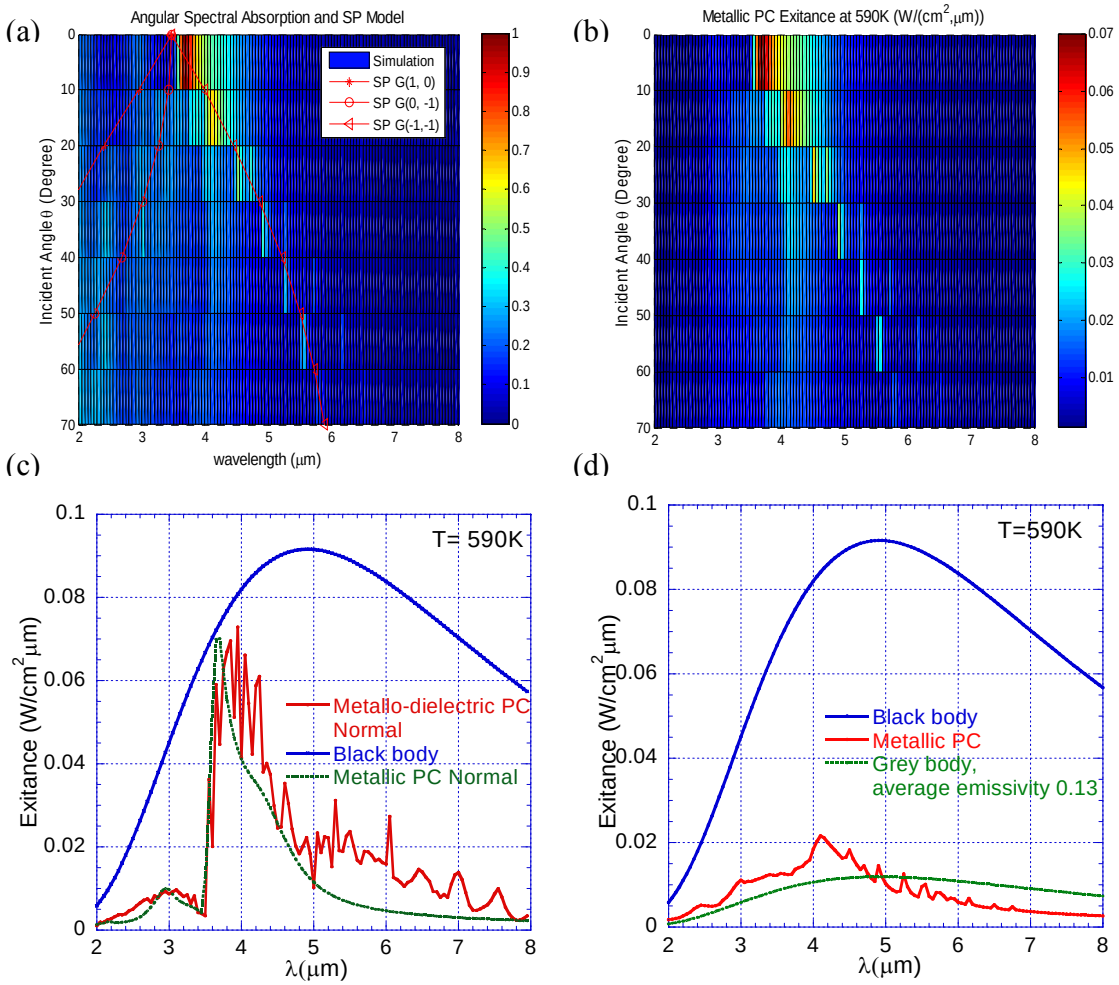

Figure 2.5 (a) Spectral absorption as a function of wavelength for different angles of incidence for the metallic PC with triangular lattice symmetry. The shading corresponds to the magnitude of absorption. The spectral absorption is averaged over s, p polarization and ϕ=0°, 30°. (b) Spectral exitance for different angles of incidence for the metallic PC with triangular lattice symmetry. The temperature is 590K. The shading corresponds to the magnitude of exitance. (c) Normal exitance of both metallic and metallodielectric PC compared to that of black body at 590K. (d) Integrated exitance over the emission angles (0-70°) of the metallic PC at 590K versus the black body exitance at the same temperature.

The exitance of a grey body at 590K with average emissivity of metallic PC is also calculated.

dimensional plot [Fig 2.5 (a)]. As the angle (θ) shifts away from normal, the absorption peak splits and shift to both shorter and longer wavelengths from the wavelength of the normal incidence absorption peak. The weak absorption peaks staying near 4 μm as the incident angle varies from 0° to 70°, causes a weak bifurcation in the two dimensional plot, and are from the absorption for azimuthal angle of 30°. We expect that more accurate sampling of azimuthal angles (ϕ) will smoothen the area between the bifurcation.

The simulated absorption [Fig 2.5 (a)] and spectral exitance at the temperature of 590K [Fig 2.5 (b)] shows most interestingly that the PC emits at both longer and shorter wavelengths as the emission angle is varied away from the normal direction. A significant exitance peak remains around 4μm at different angles of emission [Fig 2.5 (b)]. Due to the blackbody spectral exitance at 590 K having a maximum at 4.9 μm and reduced intensity at shorter wavelengths, the PC exitance at the shorter wavelength (λ<4 μm) is strongly reduced.

In the normal direction the PC has a simulated exitance [Fig 2.5 (c)] strongly peaked at ~3.7 μm with a narrow half-width of ~0.35 μm, The simulated spectral exitance in the normal direction is remarkably strong and almost reaches the black body curve. The strong normal direction exitance suggests that photons are suppressed in the long wavelength regime and enhanced in the allowed band for the small angles.

The spectral absorption $A_{avg}(\lambda)$ of the PC is obtained by integrating $A(\lambda,\theta)$ over the hemisphere from θ=0° to 70° at 10° intervals,

$$A_{avg}(\lambda) = \frac{A(\lambda,\theta=0^{\circ})\cdot(1-\cos 5^{\circ}) + \sum_{\theta=10^{\circ}}^{\theta=70^{\circ}}\left(A(\lambda,\theta)\cdot\sin\theta\cdot\cos\theta\right)}{(1-\cos 5^{\circ}) + \sum_{\theta=10^{\circ}}^{\theta=70^{\circ}}\left(\sin\theta\cdot\cos\theta\right)} \qquad (2.3)$$

The first term in the numerator represents the area of the hemispherical cap (around the normal direction) multiplied by the absorption. The integration was done in 10° increments; hence the first term is integration from -5° to +5°. For off-normal directions the integrated exitance [Fig 2.5 (d)] was calculated by combining (1) and (3). The hemispherical exitance [Fig 2.5 (d)] is much weaker than the black-body curve since the PC emits a range of wavelengths. The PC redistributes the emission at different wavelengths into different emission angles.

We obtained the average emissivity of the PC (e) by averaging $A_{avg}(\lambda)$ over all the calculated wavelengths $e = \langle A_{avg}(\lambda) \rangle$ to obtain e~0.17. We then compare [Fig 2.5 (d)] the hemispherical exitance of the PC with a grey body have the same emissivity (e~0.17) as the PC.

The intensity and width of the absorption can be increased by enlarging the size of the holes to R/a=0.35 [Fig 2.6]. The absorption resonance has broader maxima around 4 μm, and exhibits a similar variation with angle. The cut-off wavelength λ_c (3.42R) of the waveguide mode in large hole (R/a=0.35) is greater than the lattice constant (a=4μm) thus the lattice array is not a sub-wavelength structure anymore. There is a propagating waveguide mode inside the cylindrical cavities at λ~4.79 μm in addition to the surface plasmon mode at 4 μm

that causes broad absorption. PCs with broad absorption peak are promising candidates for broad band mid infrared (3 - 6 μm) applications.

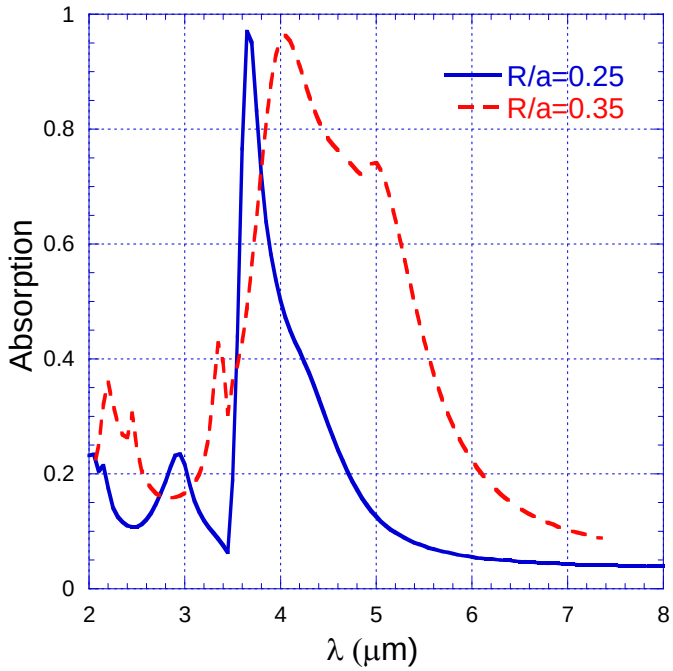

Figure 2.6 Absorption of the metallic PC with holes radius of R=0.25a and R=0.35a.

We perform similar simulations for the metallodielectric PC that has been studied previously [4]. Here a sub-wavelength array of holes in a thin Pt layer of thickness d_1~0.1μm is on top of a silicon photonic crystal of the same period with thickness of d_3~8μm, thereby forming PCs in both the metal and silicon substrate. A thin layer of SiO_2 of thickness d_2 is formed between the metal and Si to prevent inter-diffusion. The silicon PC resides on an n-doped bulk Si substrate [4]. The electric fields can penetrate into the Si PC and substrate, a significant difference from the metallic PC.

Scattering matrix simulations of the absorption of the metallodielectric PC [Fig 2.7] exhibit a very strong absorption peak (reaching 0.9) at a wavelength near the lattice constant

(a) at normal incidence. There are sub-peaks in the absorption related to the plasmon modes at the metal-Si interface. The silicon photonic crystal in the metallodielectric PC behaves as a two-layer material with a smaller effective refractive index in the upper layer (d_3) on top of the much thicker silicon substrate. Multiple reflection peaks occur due to multiple reflections within the layered structure leading to absorption sub-peaks and an overall broader absorption peak in the metallodielectric PC, than the metallic PC [Fig 2.7].

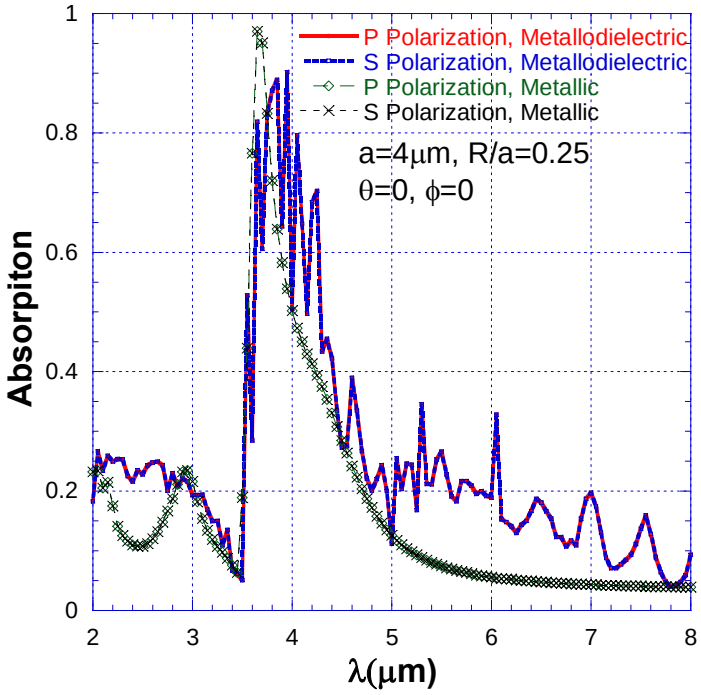

Figure 2.7 Absorption as a function of wavelength, for both 2d metallodielectric and 2d metallic PC, with triangular lattice symmetry. The incident radiation is in the normal direction.

At off-normal angles the absorption peak splits and shifts to both longer and shorter wavelengths [Fig 2.8 (a)]. There is a significant absorption peak remaining at λ~a (a=4μm) when the angle of incidence is varied from 0 to 70°. The angular absorption of the

metallodielectric PC is similar to that of metallic PC [Fig 2.5 (a)], except that the absorption peak remaining at λ~a (a=4μm) is considerably stronger.

The hemispherical simulated spectral exitance (at T=590K), [Fig 2.8 (b)] displays peaks near 4 μm and a weaker peak near 5 μm. By averaging the integrated exitance over all the wavelengths we obtain an emissivity e=0.22 for the metallo-dielectric PC. Similar to the metallic PC, the normal spectral exitance of the metallodielectric PC involves a narrow wavelength band near the peak of the absorption profile [Fig 2.7].

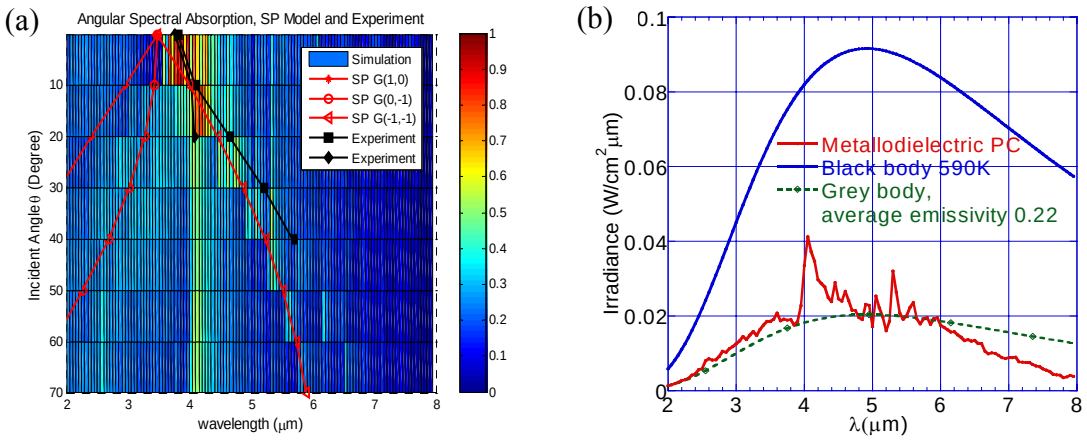

Figure 2.8 (a) Spectral absorption as a function of wavelength for different angles of incidence for the metallodielectric PC with triangular lattice symmetry. The shading corresponds to the magnitude of absorption. The spectral absorption is averaged over s, p polarization and ϕ=0°, 30°. The experiment results are included. (b) Integrated exitance of the metallodielectric PC at 590K over the incidence angle (0-70°) versus the exitance of the black body at the same temperature. The exitance of a grey body at 590K with average emissivity of metallodielectric PC is calculated.

When compared with a grey body [Fig 2.5 (d)], the metallic PC exhibits some decrease in exitance in the long wavelength regime accompanied by an increase in exitance

at wavelengths near the absorption resonance ($\lambda \sim 4$ μm) and even at shorter wavelengths ($\lambda < 4$ μm). Alternatively the metallodielectric PC shows some decrease in long wavelength exitance in conjunction with an increase in exitance in the high absorption band ($\lambda \sim 4$ μm) [Fig 2.8 (b)]. Both metallic and metallodielectric PC do exhibit photon redistribution. However there is still significant emission into all wavelengths.

The physics underlying thermal emission is that inside the PC the lattice vibrations (at a temperature T) are in thermal equilibrium with the photon states that are described by the density of photon states inside the PC. In addition photons can be transported from the bulk to the PC surface with a frequency dependent group velocity. The photon DOS and the group velocity both describe the microscopic thermal emission process [15]. Photons are emitted and absorbed from the surface of the PC consistent with thermal balance. There is diffraction at the surface of the PC, where photons emitted with wave-vector k will couple to Fourier components of the electric field at the surface (with components G) since the surface is periodic, and result in emission with wave-vectors k+G. Here G is a reciprocal lattice vector of the PC. This redistributes the radiation intensity from the spectrum inside the PC into one with strong angular dependence outside the PC. Effectively, the PC channels photons of specific wavelengths into well defined angular bands. To obtain more useful exitance in the band of interest, one may enhance the surface waves by manipulating the surface structure. A promising approach is to use a patterned metal surface with circular concentric grooves surrounding a single aperture, which has been demonstrated to have emittance and beaming with small angular divergence [16]. An alternative strategy is to retain a periodic structure

but create defects (protrusions) neighboring to the holes and thereby modifying the surface wave behavior in the structure.

Discussion and Surface plasmon model

The principal features of the angle-dependent absorption and exitance can be understood from a simple surface plasmon model [17]. Theoretical analysis has established that sub-wavelength hole arrays exhibiting extraordinary transmission [18, 19] support a surface mode that has high electric field in the air half-space and in the holes [20]. This surface mode has dispersion similar to the surface plasmon mode at metal-dielectric interfaces. Hence an analysis with a simple surface plasmon model can yield valuable insight.

For a triangular lattice (of lattice constant a), the reciprocal lattice vectors are,

$$G_1 = \frac{2\pi}{a}(1, -\frac{1}{\sqrt{3}}); G_2 = \frac{2\pi}{a}(0, \frac{2}{\sqrt{3}}) \tag{2.4}$$

Surface plasmons at a metal dielectric interface films are longitudinal modes propagating along the surface with exponentially decaying amplitude away from the interface, and have a dispersion relation,

$$k_{sp} = \frac{\omega}{c}[\frac{\varepsilon_1 \varepsilon_2}{\varepsilon_1 + \varepsilon_2}]^{\frac{1}{2}} \tag{2.5}$$

ε_2 is the real part of the metal dielectric function that is negative, and large in magnitude, for IR frequencies. ε_1 describes the dielectric media. Since the surface plasmon dispersion lies

below the incoming light line for any angle of incidence (θ), incoming light cannot directly generate surface plasmons on a smooth surface.

When an incident light of angular frequency ω, impinges on the patterned surface at an angle θ, it can couple to a surface plasmon at the air/metal interface through a reciprocal lattice vector,

$$\frac{\omega}{c}\sin\theta\,\mathbf{i} + \mathbf{G} = \mathbf{k}_{sp} \tag{2.6}$$

By combining the dispersion relation (5) with this momentum conservation condition (6), we get the eigen-value equation for the surface plasmon frequencies,

$$[\frac{\varepsilon_1\varepsilon_2}{\varepsilon_1+\varepsilon_2}] = [\sin\theta\cos\phi \pm i\frac{v_0}{v}]^2 + [\sin\theta\sin\phi \mp i\frac{1}{\sqrt{3}}\frac{v_0}{v} \pm j\frac{2}{\sqrt{3}}\frac{v_0}{v}]^2 \tag{2.7}$$

Where v_0=c/a. The fundamental surface plasmon mode (i=1,j=0 or i=0,j=1) is predicted to occur at a wavelength of $(\sqrt{3}/2)$a. As the angle θ varies away from the normal, this model predicts an increase of the wavelength of the absorption maximum coupled with the appearance of modes at shorter wavelength [Fig 2.8 (a) and Fig 2.5 (a)]. The primary calculation results could be described by the surface plasmon model. There is good agreement in the increase in the wavelength of the longer wavelength mode between the SP model and scattering matrix simulation. In the two dimensional PC in this paper, the absorption maximum are strongly dependent on the incident angles and caused by the surface plasmon-like mode in the PC as discussed in the surface plasmon model.

This surface mode decays evanescently in the interior of the holes. The resonant surface mode wavelength exceeds the cutoff (3.42*R*) for a circular aperture. All waveguide modes within the aperture are evanescent. The decaying propagation constant of the waveguide mode is

$$\gamma = \frac{1}{l_d} = 2\sqrt{\left(\frac{k_{nr}}{R}\right)^2 - \left(\frac{2\pi}{\lambda}\right)^2} \tag{2.8}$$

where k_{nr} is the *r*th zero of the nth Bessel function. The TE11 mode (k_{11}=1.84) has the largest decay length l_d. The predicted value of l_d/a is 0.15 from (8) at the resonant wavelength. The hole depth $d_1 >> l_d$, since d_1/a~0.5. Hence evanescent modes inside the aperture are effectively absorbed. The resonant mode inside the holes has large oscillating fields inside the cylinder surface that induce large oscillating currents on the cylinder surface and dissipate energy from the incident wave.

The mechanism of absorption in the 3-d woodpile photonic crystal is somewhat different. The absorption is caused by a propagating Bloch mode that transmits through the different layers of the woodpile structure [21]. This Bloch mode is a waveguide-like mode that couples through different layers of the metallic PC [21]. Since the absorption is caused by a propagating Bloch mode at a resonant wavelength, the absorption maximum is insensitive to the incident angle. In the woodpile structure also, the oscillating fields of the resonant mode inside the structure cause oscillating currents induced on the surface of the metallic PC. The oscillating currents on the surfaces of the metallic structure cause dissipation and remove energy from the incident wave. The absorption and oscillating

currents occur in the near surface region of the 2-d PC and through the entire thickness of the woodpile structure.

In comparison we find that the absorption maxima in the 2-d PC does shift with incident angle more significantly than in the 3-d woodpile structure. However the the band edge where the absorption drops from the long-wavelength limit does shift to longer wavelengths, with increasing angle of incidence [9] for the 3-d woodpile structure, somewhat similar to the behavior of this 2-d PC. TPV devices from both 2-d and 3-d structures need to consider these trade-offs of angular behavior with the complexity of the structure.

The shifts of the exitance peaks with angle were measured for the metallo-dielectric PC with a Fourier transform infrared spectrometer (FTIR) fitted with an external emission port. The positions of the measured exitance peaks are compared with the simulations and SP model predictions [Fig 2.8 (a)]. There is good agreement between the prediction of surface plasmon modes ((0,-1), (1,0), (1,1)) by the SP model and the measurement of surface plasmon modes at incidence angles from 0 to 40°.

We investigate the field distribution in the metallic PC within the hole [Fig 2.9(a)] and at the surface [Fig 2.9 (b), (c)] at the wavelength of the absorption peak. The decay length of the field

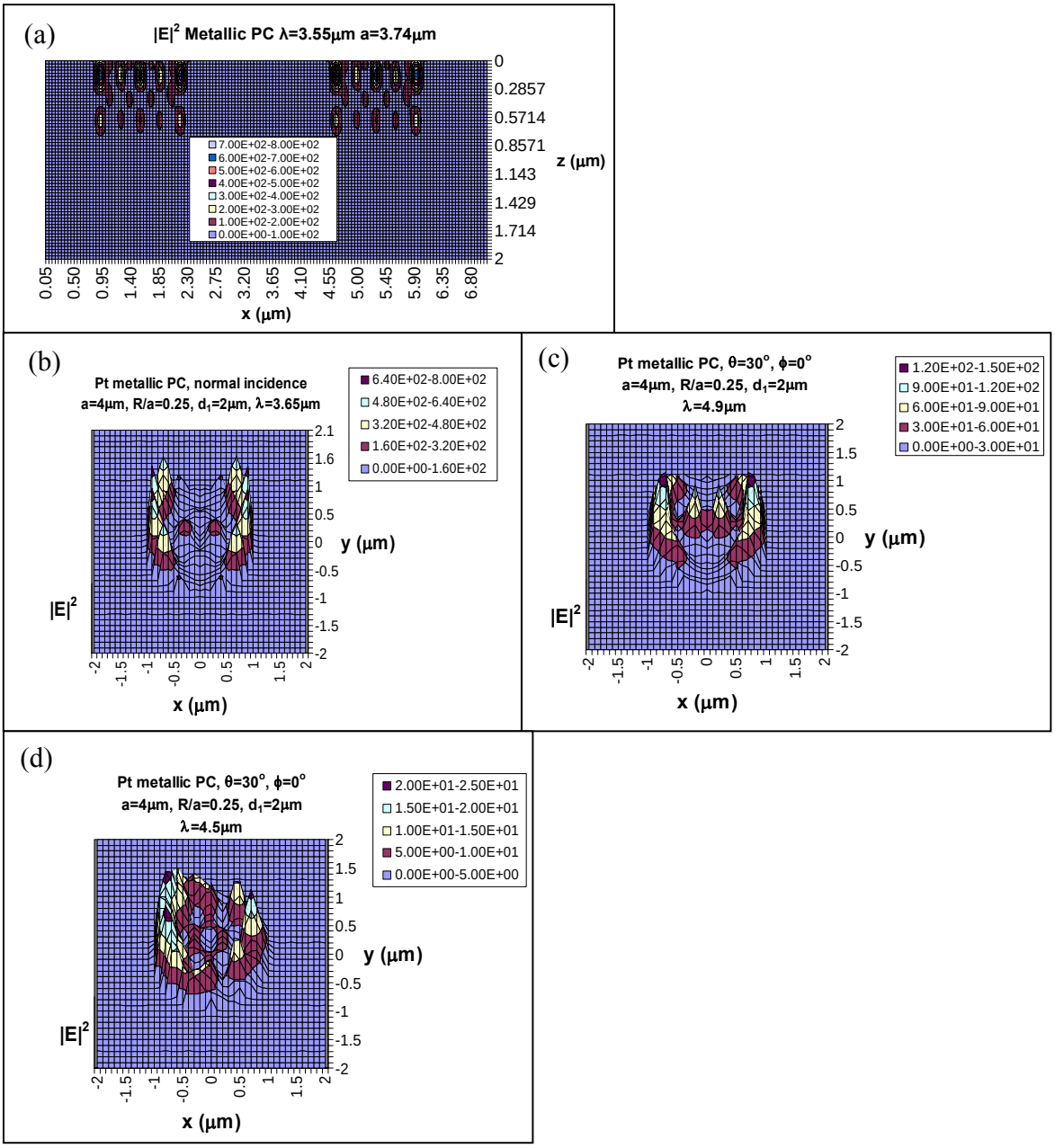

Figure 2.9 (a) Field distribution in x-z plane of the metallic PC (a=3.74μm) with normal incidence shown for two neighboring holes. The resonance wavelength is 3.55μm. Also shown in (b) (c) (d) are three-dimensional views of the field distribution just below the surface of one hole. (b) The incidence is in the normal direction. The wavelength is 3.65μm. (c) The incident angle is 30° and the azimuthal angle is 0°. The wavelength is at resonance wavelength of 4.9μm. (d) The incident angle is 30° and the azimuthal angle is 0°. The wavelength (4.5 μm) is at not at resonance.

is ~0.8μm inside the hole [Fig 2.9 (a)], close to the predicted value (~0.6μm) of the decaying waveguide mode from (8). The field intensity is very strongly enhanced by factors exceeding 100 at the rim of the holes. The high field intensities extend a short distance inside the hole (<0.4 μm). In normal incidence at the resonance wavelength of 3.65μm [Fig 2.9 (b)], the field intensities at the surface exhibit approximately quadrupolar distribution with intensity maxima 30° away from the x-axis, in between the centers of the holes. When the incident angle increases to 30° and at the resonance wavelength of 4.9μm [Fig 2.9(c)], the field intensity at the surface exhibit approximately dipolar distribution with large enhancement (~150) at the rims of the hole that is lower than that at normal. We also investigate the field distribution at the surface at off-resonance wavelength (4.5μm) for incident angle of 30° [Fig 2.9 (d)]. The maximum field intensity is merely ~3% of that at normal so that induced charges are weak. There is no well-defined modal distribution. At both incident angles (normal and 30°) at the resonance wavelength, the field intensity maximum from the scattering matrix simulations are due to the induced charges at the rim of the hole. Such induced charges are expected from a surface plasmon like mode - which connects the scattering matrix simulation to the surface plasmon model- and describes the angular

dependence of the absorption peaks in the surface plasmon model [Fig 2.5 (a)]. The appearance of strong induced charges at the hole rims provide indirect support for the surface plasmon model.

In the metallodielectric PC, when the incidence angle increases from 0° to 70°[Fig 2.8 (a)], the first absorption peak stays near λ~a (a=4.0 μm). At θ=0°, the second absorption peak starts

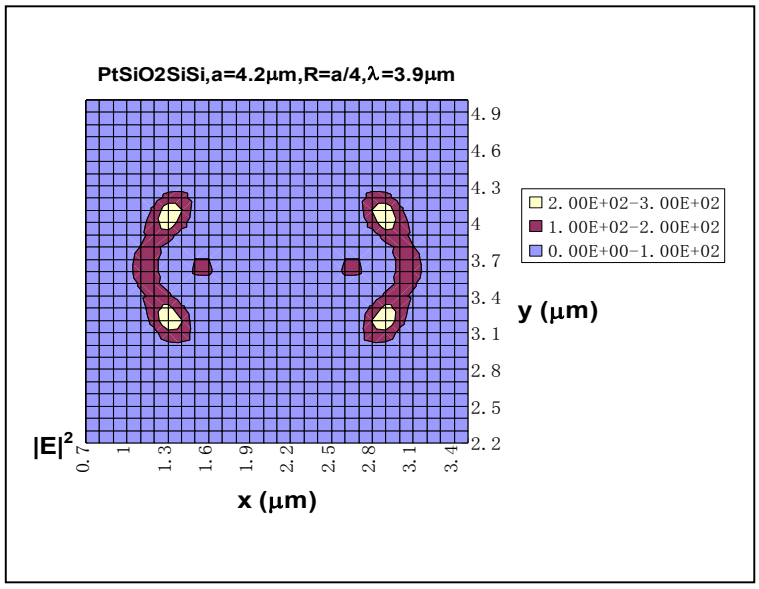

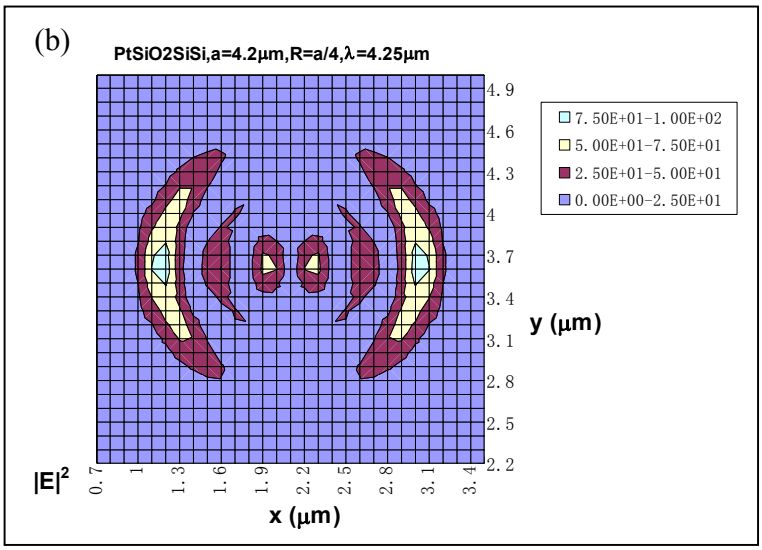

Figure 2.10 Field distribution in the x-y plane just below surface of one hole in the metallodielectric PC (a=4.2μm) with normal incidence. (a) The wavelength is 3.90μm. (b) The wavelength is 4.25μm.

from 3.7 μm, and shifts to longer wavelength. To understand the different behavior of the two absorption peaks, we simulate the field distribution at the surface of the metallo-dielectric PCs and find different mode symmetries. Fig. 2.10 (a) shows the field distribution at the wavelength of 3.7 μm. The field is concentrated at the rim of the hole with field maxima [Fig 2.10(a)] in a quadrupolar distribution at the rim of the hole. Similar distribution is found in the metallic PC. The field maxima are oriented along the first shell of G vectors and can couple to incident waves at different angles of incidence. Fig 2.10 (b) shows the field distribution for the mode near $\lambda \sim a$. The field concentrates at the rim of the hole. However, the maxima of field form a dipolar distribution at the rim of the hole. The dipolar mode does not change wavelength when the angle is changed.

Conclusions

We have investigated the angular spectral absorption characteristics of both the metallic PC and metallodielectric PC. By convolution of the black body exitance with the absorption profile of the PC, thermal exitance of the heated PC is obtained. The PC redistributes the thermal emission at different wavelengths into different emission angles. The thermal exitance of PC over all the angles is similar to a grey body with the integrated emissivity of PC. We observe redistribution of photons from outside of the allowed spectral region into the allowed spectral region. We also investigate the surface plasmon models to find the absorption peak wavelength of the PC. There is good agreement between surface plasmon model and simulated absorption using scattering matrix method.

Acknowledgements

We thank A. Greenwald, D. Zhou and L. Garcia for many helpful discussions. We acknowledge the support from the National Science Foundation under grant Nos.ECS-06013177 at Iowa State University and DMI-0450397 at ICX-Photonics (formerly Ion-Optics). The Ames Laboratory is operated for the Department of Energy by Iowa State University under Contract No.DE-AC0207CH11385.

References

1. S.Y. Lin, J.G. Fleming, and I. El-Kady, "Three-dimensional photonic-crystal emission through thermal excitation", Opt. Lett. **28**, 1909-1911 (2003).
2. I. Puscasu, M. Pralle, M. McNeal, J. Daly, A. Greenwald, E. Johnson, R. Biswas and C. G. Ding, "Extraordinary emission from two dimensional plasmonic-photonic crystals", J. Appl. Phys. **98**, 13531 (2005).
3. I. El-Kady, W. W. Chow, J. Fleming, "Emission from an active photonic crystal", Phys. Rev. B **72**, 195110 (2005).
4. R. Biswas, C.G. Ding, I. Puscasu, M. Pralle, M. McNeal, J. Daly, A. Greenwald, E. Johnson, "Theory of subwavelength hole arrays coupled with photonic crystals for extraordinary thermal emission" , Phys. Rev. B. **74**, 045107 (2006).
5. S. Y. Lin, J. Moreno, and J. G. Fleming, "Three-dimensional photonic-crystal emitter for thermal photovoltaic power generation", Appl. Phys. Lett. **83**, 380-382 (2003).
6. H. Sai, H. Yugami, "Thermophotovoltaic generation with selective radiators based on tungsten surface gratings" Appl. Phys. Lett. **85**, 3399-3401 (2004).

7. I. Čelanović, N. Jovanović, and J. Kassakian, "Two-dimensional Tungsten Photonic Crystals as Selective Thermal Emitters" Appl. Phys. Lett. 92, 193101 (2008).
8. M. Florescu, H. Lee, I. Puscasu, M. Pralle, L. Florescu, D. Z. Ting, J. P. Dowling, "Improving solar cell efficiency using photonic band-gap materials", Solar E**ne**rgy Materials and Solar Cells **91**, 1599-1610 (2007).
9. J. Fleming, S. Lin, I. El-Kady, R. Biswas, and K. M. Ho, "All metallic absolute photonic band gap three-dimensional photonic crystals for energy applications", Nature **417**, 52-55 (2002).
10. R. Biswas, D. Zhou, I. Puscasu, E. Johnson, A. Taylor and W. Zhao, "Sharp thermal emission and absorption from conformally coated metallic photonic crystal with triangular lattice" , Appl. Phys Lett. **93**, 063307 (2008).
11. J.H. Lee, C.H. Kim, Y-S. Kim, K.M. Ho, K.Constant, and C.H. Oh, "Three-dimensional metallic photonic crystals fabricated by soft lithography for midinfrared applications", Appl. Phys. Lett. **88**, 181112 (2006).
12. Z. Y. Li and L. L. Lin, "Photonic band structures solved by a plane-wave based transfer matrix method," Phys. Rev. E 67, 046607 (2003).
13. R. Biswas, S. Neginhal, C. G. Ding, I. Puscasu, E. Johnson, "Mechanisms underlying extraordinary transmission in sub-wavelength hole arrays", J. Opt. Soc. of America B 24, 2489-2596 (2007).
14. C. Luo, A. Narayanaswamy, G. Chen, and J. D. Joannopoulos, "Thermal radiation from Photonic crystals a direct calculation", Phys. Rev. Lett. 93, 213905 (2004).
15. M. Florescu, K. Busch, J. P. Dowling, "Thermal radiation in photonic crystals", Phys. Rev. B **75**, 201101 (2007).

16. H. J. Lezec, A. Degiron, E. Devaux, R. A. Linke, L. Martin-Moreno, F. J. Garcia-Vidal, and T. W. Ebbesen, "Beaming light from a subwavelength aperture," Science 297, 820–822 (2002).

17. H. Raether, *Surface Plasmons*, Springer Tracts in Modern Physics, vol. **111**, Springer-Verlag, Berlin, 1988.

18. T. W. Ebbesen, H. J. Lezec, H. F. Ghaemi, T. Thio, and P. A.Wolff, "Extraordinary optical transmission through subwavelength hole arrays," Nature **391**, 667-669 (1998).

19. L. Martin-Moreno, F. J. Garcia-Vidal, H. J. Lezec, K. M.Pellerin, T. Thio, J. B. Pendry, and T. W. Ebbesen, "Theory of extraordinary optical transmission through subwavelength hole arrays," Phys. Rev. Lett. **86**, 1114-1117 (2001).

20. J. Pendry, L. Martin-Moreno, and F. J. Garcia-Vidal, "Mimicking surface plasmons with structured surfaces," Science **305**, 847-848 (2004).

21. Z. Y. Li, I. El-Kady, K. M. Ho, S. Y. Lin and J. G. Fleming, "Photonic band gap effect in layler-by-layer metallic photonic crystals," J. Appl. Phys. **93**, 38-42 (2003).

CHAPTER 3 PHOTONIC CRYSTAL BASED TUNGSTEN FILAMENT FOR HIGH INTENSITY LIGHT BULBS

Introduction

It is widely acknowledged that the efficiency of light bulbs with tungsten filaments is very low since a large portion (>90%) of the energy is radiated as heat. Using recent advances in photonic crystals and sub-wavelength hole arrays we show that it is possible to considerably increase the lifetime and the brightness of such incandescent filaments.

Sub-wavelength arrays of holes in thin metal sheets exhibit the extraordinary transmission phenomenon when the wavelength of incoming light is close to the lattice spacing [1-12]. In parallel with this phenomenon there has been a very active study of how metallic and metallo-dielectric photonic crystals enhance and modify the thermal radiation spectrum. We have previously designed a metallo-dielectric photonic crystal where a sub-wavelength array of holes in a thin metal sheet resides on a semiconducting photonic crystal. This converts the extraordinary transmission into a sharp absorption within the weakly absorbing photonic crystal. When heated this structure exhibits a narrow thermal emission at infrared wavelengths.

We propose a new all-metallic photonic crystal structure with a remarkable absorption at a tunable wavelength controlled by the lattice spacing (a), and a consequently high intensity of emission band. The structure consists of a triangular lattice of cylindrical pits of radius R and depth d_1 etched into a tungsten film. There is a uniform tungsten

substrate of thickness d_4 below the triangular lattice of holes, so that the tungsten structure's thickness is d_1+d_4 [Fig. 1]. Since tungsten is absorbing the precise value of d_4 is not critical for the design as long as d_4 is several wavelengths thick.

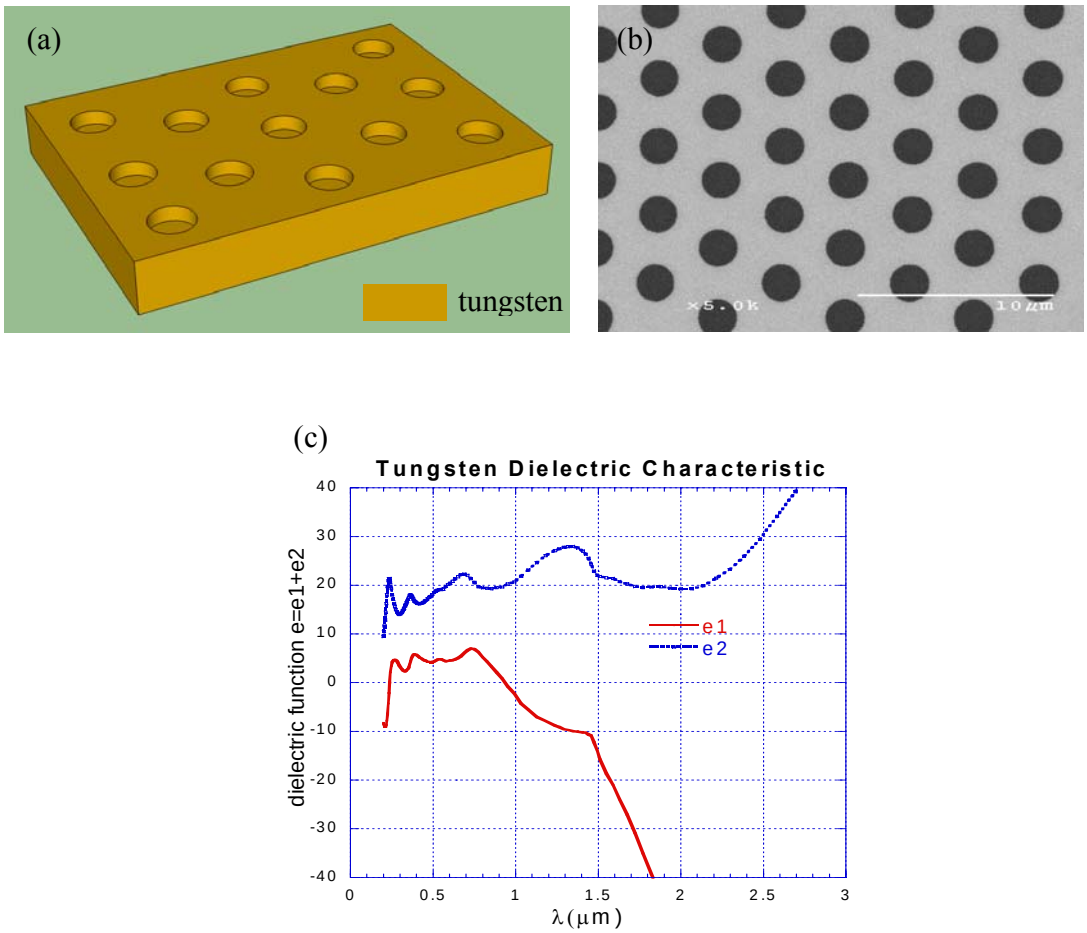

Figure 3.1 (a) Schematic of metallic photonic crystal structure, with the thicknesses of the photonic crystal is d_1 and substrate. The pitch size of the holes array is a. The radius of the hole is R. The structure is composed of tungsten. (b) SEM image of a 2-d triangular lattice of holes. (c) Experimentally measured real and imaginary parts of the dielectric function of tungsten as a function of the wavelength.

Simulation and Results

The reflection (R) and transmission (T) from this array was calculated with the well-established scattering matrix method, where Maxwell's equations were solved in a plane wave basis for each frequency at a time. Diagonalization of the transfer matrix within each layer provides the eigenmodes and propagation wavevectors and the scattering matrices within each layer. By demanding continuity of the fields at each interface and using standard recursion relations the scattering matrix of the entire structure was determined. With the initial conditions of waves incident from the left, the reflection and transmission for each frequency and incident angle was found from which the absorption $A = 1-R_{ns}-T_{ns}$ was computed, where R_{ns} and T_{ns} are the nonspecular reflection and transmission respectively. The simulations are performed with the frequency-dependent dielectric functions of tungsten ($\varepsilon_1(\omega)$, $\varepsilon_2(\omega)$) inferred from low temperature tungsten films [4], which exhibit considerable absorption at optical wavelengths. This one-layer patterned tungsten films is considerably simpler to fabricate and offers higher performance than the more complex layer-by-layer structure that requires 4 patterned layers to complete one unit cell.

We first simulate the lattice spacing at normal direction in the optical range ($a=0.6\mu$) for medium size holes ($R/a=0.35$). A narrow reflection dip is observed for small depths d_1 of 0.1μ. By increasing d_1 to 0.2μ, the simulated non-specular reflectance [Fig 3.2(a)] produces a major reflection dip at $\lambda\sim0.6\mu$ that reaches zero. R_{ns} decreases continuously from the long wavelength value (~0.95) to this minimum at 0.6μ before increasing again at shorter wavelengths. The dip is not as sharp as found in sub-wavelength arrays of holes since tungsten has the real component of the dielectric function positive between 0.2-0.95μ [Fig

3.1(c)], quite different from a typical metal. The kink at 1.5μ is due to the kink of the ε_1 of W at this wavelength, that arises from the electronic band structure of W. Since the transmission T is very small through the thick tungsten structure ($<10^{-4}$), the absorption A~1-R_{ns} shows a pronounced peak at λ~a (0.6μ) reaching a value of 1 [Fig. 2(b)].

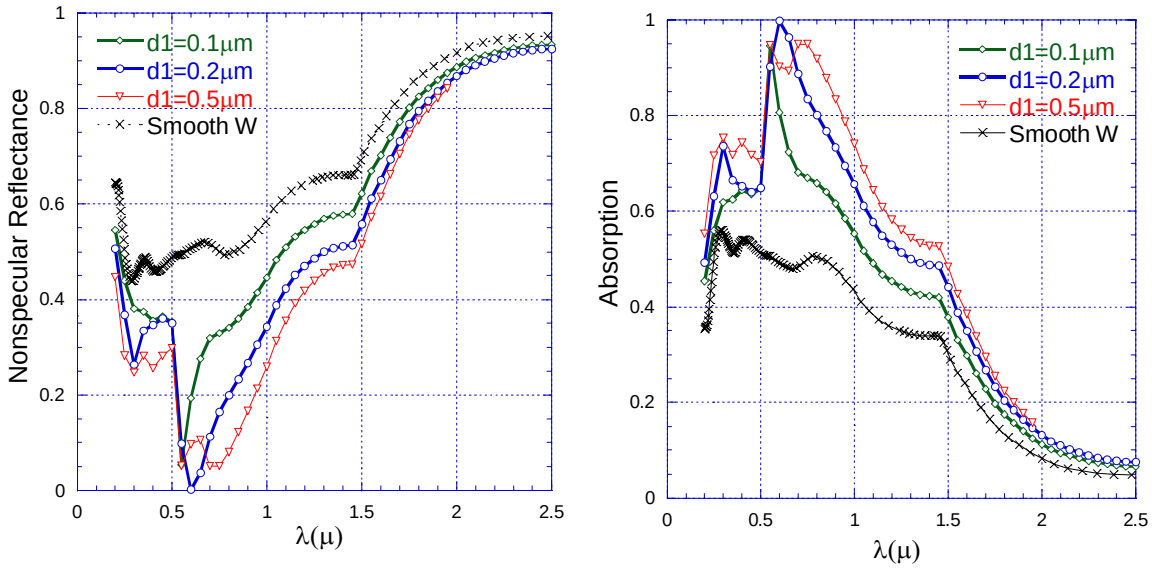

Figure 3.2 Calculated normal non-specular reflectance (a) and absorption (b) of a triangular lattice of holes with lattice constant a=0.6 μm, radius r=0.21μm, r/a=0.35 and substrate thickness d_4=10 μm, as a function of the photonic crystal thickness (d_1) that varies from 0.1 μm to 0.5 μm. The reflectance and absorption of a smooth tungsten film is shown for comparison.

We also calculated the R_{ns} expected for a smooth tungsten film with these frequency dependent dielectric functions [Fig 3.2(a)]. For smooth W, at optical wavelength range, the R_{ns} ~ 0.45-0.55 implies an absorbance A~ 0.55-0.45. The periodically textured W film has an absorbance that is consistently higher than the uniform W film at all wavelengths larger than 0.25μ, and more than 20% larger at the all-important optical wavelengths.

Further, we calculated the absorption of a triangular lattice of holes on a tungsten substrate [Fig 3.3], as a function of incident angle θ in s- and p-polarizations with the configuration (a=0.6 μm, R/a=0.35, d_1=0.2 μm, d_4=10 μm) that optimizes the absorption of triangular lattice. We observed that at normal incidence, the same absorption peak (~1.0) exists in both polarizations at the wavelength corresponding to the lattice spacing a. At off-normal directions, the photonic crystal redistributes its absorption at different wavelengths for different incidence angle θ.

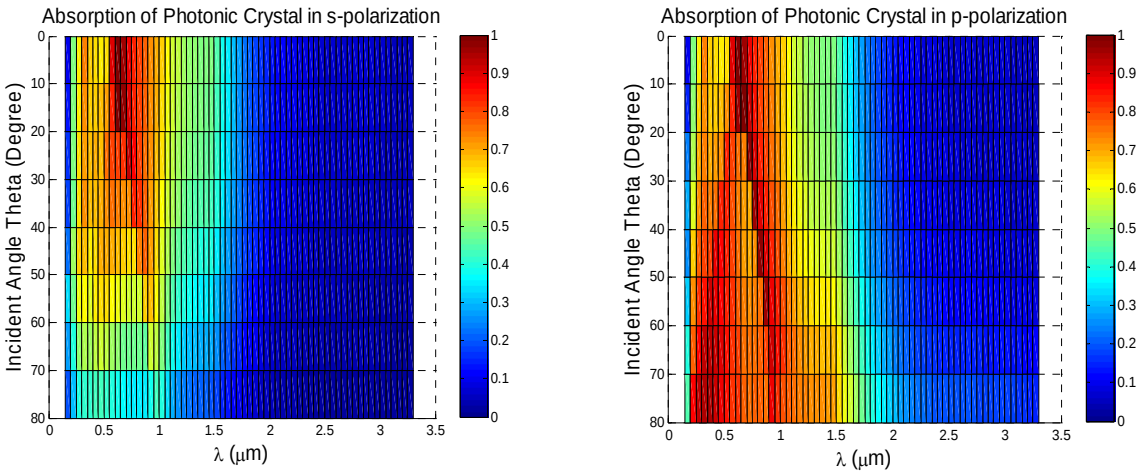

Figure 3.3 Calculated two-dimensional graph of the absorption of the tungsten photonic crystal in s- and p-polarizations as a function of the wavelength and incident angle θ. The PC thickness d_1 is 0.2 μm. Other parameters are kept same as the photonic crystal in Figure. 2.

In both polarizations, the absorption peak shifts away from the original wavelength that is the same as lattice spacing a at normal incidence when θ increases. In p-polarization, two absorption peaks develop for off-normal incidence [Fig 3.3 (b)]. The long-wavelength absorption peak moves continuously to longer wavelength with A~1.0 for θ<60°. The shorter wavelength peak increases its strength at large angles (θ>60°), moving continuously to

shorter wavelengths. The absorption in p-polarization is much larger than in s-polarization for large incidence angles. The absorption of the photonic crystal approaches the broader black-body curve when all emission angles are considered.

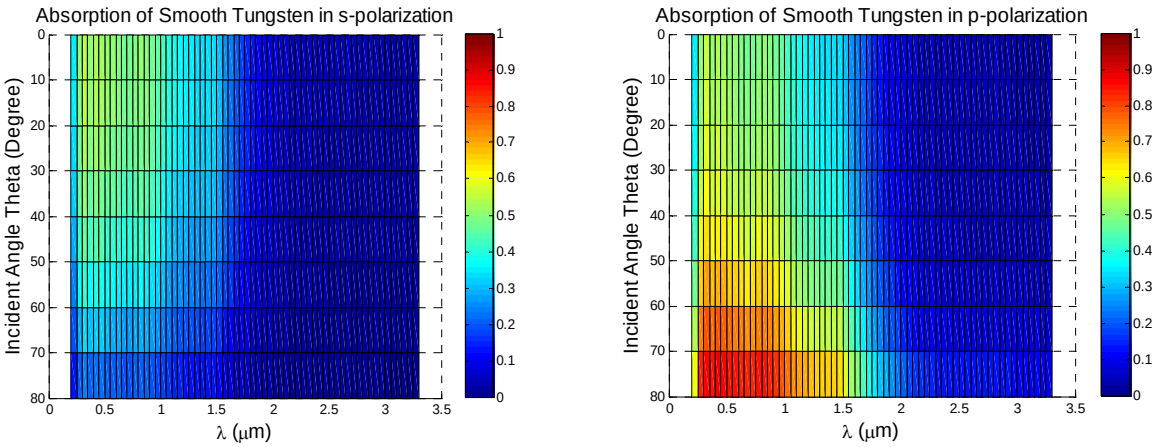

Figure 3.4 Calculated two-dimensional graph of absorption of a smooth tungsten film in s- and p-polarizations as a function of the wavelength and incident angle θ.

For comparison, we also calculated the absorption of smooth tungsten film as a function of incident angle θ for both polarizations [Fig 3.4]. At normal incidence the peak absorption is ~0.5 for both polarizations. The smooth tungsten film has a similar absorption distribution against the wavelength in both polarizations when the incident angle is lower than 40°, and shows much smaller absorption than that of photonic crystal at the same θ. However, when θ increases beyond 40°, the smooth tungsten film exhibits very strong absorption (A~0.9) below 1.5μm in p-polarization. This is due to the large transmission and vanishing reflection of tungsten for p-polarization at wavelengths where tungsten is non-metallic ($\varepsilon_1>0$). The corresponding Brewster angle is ~74° considering the real part of the dielectric function and neglecting the dielectric loss of tungsten. The photonic crystal

structure has much larger absorption at optical wavelengths than the smooth tungsten film, especially for near-normal incident angle θ.

Since bulk tungsten has a high melting point (3695 K) and significant absorption (~0.5) at optical wavelengths, it is used extensively as an incandescent light source. Hence we next compare the performance of photonic crystal with that of smooth tungsten film. We calculated the absorption $A(\theta,\lambda)$ of the tungsten PC and the smooth W film by averaging the calculated absorption ($A(\phi,\theta,\lambda)$) over s, p polarizations and ϕ=0°, 30°. Due to the lattice symmetry rotations through azimuthal angles of 60° are equivalent. The hemispherical spectral absorption $A(\lambda)$ of the PC and smooth W film [Fig 3.5(a)] is obtained by integrating $A(\lambda,\theta)$ over the hemisphere from θ=0° to 80° at 10° increments [13],

$$A(\lambda)=\frac{A(\theta=0^{\circ},\lambda)(1-\cos 5^{\circ})+\sum_{\theta=10}^{\theta=80}A(\theta,\lambda)\cdot\sin\theta\cdot\cos\theta}{(1-\cos 5^{\circ})+\sum_{\theta=10}^{\theta=80}\sin\theta\cdot\cos\theta} \tag{3.1}$$

The first term in the numerator represents the area of the hemispherical cap (around the normal direction) multiplied by the absorption. Hence the first term is integration from -5° to +5°.

The result [Fig 3.5(a)] demonstrates that the average absorption of the photonic crystal is about 20% larger than a smooth tungsten film at optical wavelengths and somewhat large for infrared wavelengths as well. According to Kirchhoff's law, the exitance is the product of the wavelength-dependent absorption and the Planck black-body exitance. Therefore, the exitance of both the photonic crystal and smooth W film could be obtained

through the product of wavelength-dependent absorption and black body spectral irradiance at specific temperature. At 2660K, typical of the temperature of an incandescent source, the thermal exitance of both photonic crystal and smooth tungsten film [Fig 3.5(b)] peaks at 0.9 μm while the thermal spectral irradiance of photonic crystal is about 25 percent larger than that of smooth tungsten between 0.9 and 1.4μm. The thermal exitance of photonic crystal at optical wavelengths is also greatly larger than a smooth tungsten film.

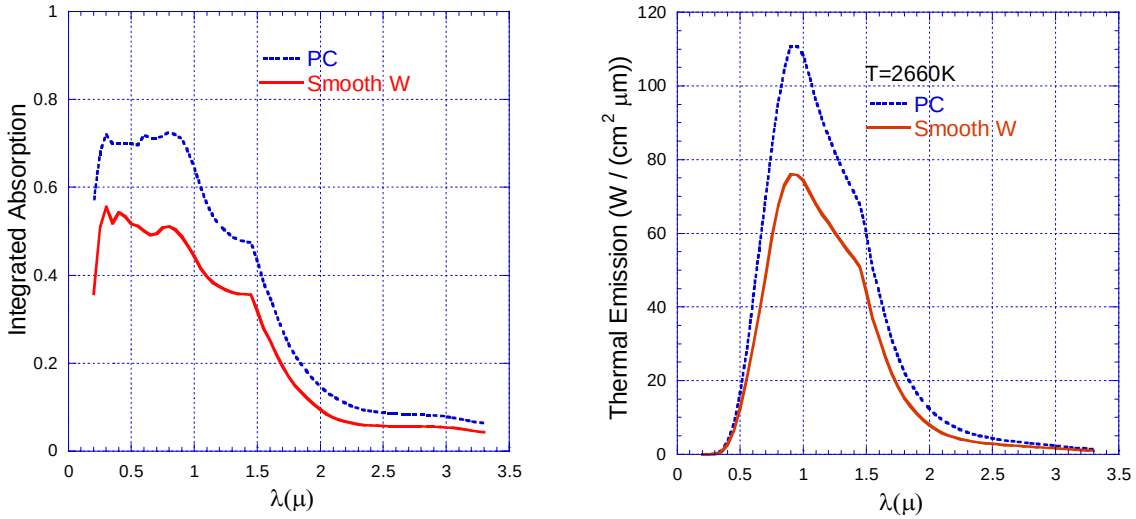

Figure 3.5 (a) Calculated average absorption of photonic crystal compared to that of smooth tungsten film. The calculated absorption is averaged over the incident angle θ from 0º to 90º, angle φ with 0° and 30°, and over both p- and s-polarizations. The parameters are kept the same as the photonic crystal in Figure. 2 (b) The simulated thermal emission density of both photonic crystal and smooth tungsten when the temperature is at 2662K. The thermal emission density is the product of absorption and blackbody emission density.

To further compare the thermal effect of the PC and smooth W, we consider typical conditions for a 100W incandescent light bulb which has a coiled tungsten filament length of L=0.58 m, and radius of r=0.0032 cm [14] equivalent to a smooth W film surface area of

S=1.17×10^{-4}m^2 at room temperature. We assume that both heat conduction loss and thermal expansion effect of PC and W film can be neglected. According to energy conservation, the total power emitted over the wavelength range of 0.2μm to 3.3μm from the filament surface should equal to the input electrical power at energy balance,

$$\Delta\lambda \cdot S \cdot \sum_{\lambda=0.2um}^{\lambda=3.3um} [A(\lambda) \cdot M_{BB}(\lambda, T)] = V^2 / R(T) \tag{3.2}$$

$\Delta\lambda$ is the wavelength interval (0.05μm) used in simulation, $M_{BB}(\lambda,T)$ is exitance of black body at temperature T, V is the root mean square (RMS) of the ac supply voltage (120V), $R(T)$ is the temperature dependent resistance of the W filament in a 100W light bulb.

The resistance $R(T)$ is simply,

$$R(T) = \frac{\rho(T)L}{\pi r^2} \tag{3.3}$$

In which $\rho(T)$ is the measured temperature-dependent resistivity of the W filament [16]. $\rho(T)$ is approximately increases linearly with temperature, similar to common metals

The operating temperatures are obtained by solving (3.2) graphically [Fig 3.6] and setting the total emitted power to equal the input electrical power. From energy balance, the operating temperature of the PC is ~2590K, compared to 2750K for the smooth W. At 2750K, the smooth W emits ~98W. The PC operates at a considerably low temperature (~160K lower) and emits ~105W, ~7% higher than the smooth W. Between the operating temperature of PC (~2590K) and smooth W (~2750), we choose 2660K as the typical of incandescent filaments through calculation.

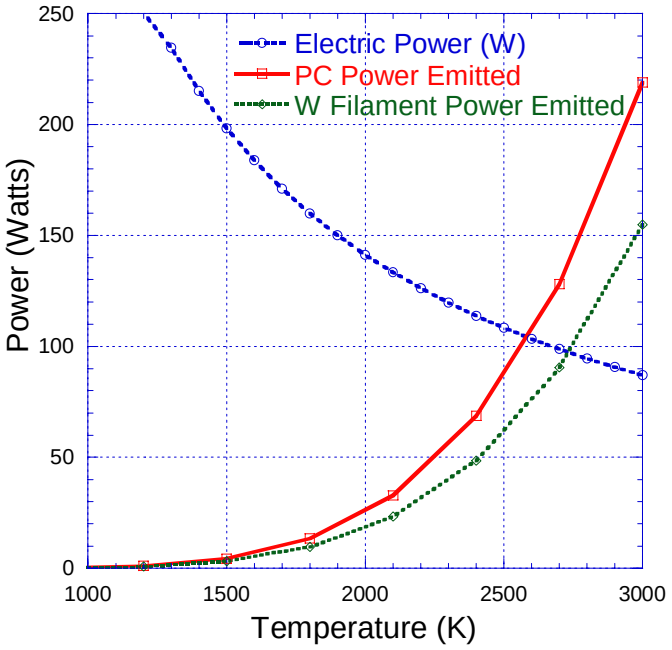

Figure 3.6 To solve graphically operating temperature of W filament where the input electrical power equals the total emitted power.

Vaporization of W from filament surface at extremely high temperature leads to the thinning of the filament, where the brittle facture might happen and results in the filament failure. The oxidation of W filament by trivial amount of air slowly leaking into the light bulb also contributes to the failure of the W filament. Both the vaporization and oxidation processes strongly depend on the operating temperature of the filament. The lower operating temperature of W filament could slow down the vaporization and oxidation processes, thus increasing the lifetime of the filament.

We next calculated the output light intensity (I, in lumens) of both photonic crystal and smooth tungsten film at 2660K using the relation

$$I = 683(lumens/W) \times S \times \int_{0.4\,\mu m}^{0.75\,\mu m} A(\lambda) \times e(\lambda) \times L_F(\lambda) d\lambda \qquad (3.4)$$

In which $A(\lambda)$ is the integrated absorption spectrum over the angle of 0 to 80°, $e(\lambda)$ is the blackbody exitance. Therefore, the product of $A(\lambda)$ and $e(\lambda)$ is the integrated exitance at a specific temperature. $L_F(\lambda)$ is the standard luminosity function [15,17] representing the human visual response.

Using the typical temperature estimated previously T=2660K, and (3.4), we estimate [18] the light output intensity of a tungsten filament to be 1960 lumens [Table 3.1]. This is ~14% higher than the widely quoted 1640 lumens for a 100 W incandescent light bulb, due to the neglect of heat conduction losses in tungsten. The tungsten photonic crystal at the same temperature, however, has a much higher output light intensity of 2740 lumens [Table 3.1]. Thus the output light intensity I of the photonic crystal is 1.4 times as large as that of smooth tungsten film.

The photonic crystal however does not reduce the fraction of energy emitted outside optical wavelengths in the infrared region. The ratio of power emitted at optical wavelengths to the total emission is 0.15, same for both structures.

The origin of the enhanced emittance lies in the extraordinary transmission effect. For thin W films (eg. d_1=0.1μ) without a substrate, a transmission peak is observed at $\lambda \sim a$. For a within the optical range this transmission peak in W is somewhat broader than typically found in metals. The extraordinary transmission mode consists of a superposition of exponentially decaying eigen-modes within the hole [19]. For thin metal sheets, ($d_1 << \lambda$) the decay is not significant. The enhanced transmission is converted into enhanced absorbance, which in turns leads to enhanced thermal emission when the structure is heated.

Table 3.1 Simulated output light intensity in the visible wavelength range of 0.4μm to 0.75μm using the luminosity function, for a smooth tungsten filament at 2660K, compared to a photonic crystal based tungsten filament. The area of the filament has been taken to be 1.17×10^{-4} m^2, typical of a 100W light bulb filament. The heat conduction loss has been neglected.

Structure	Light output (Lumens)
Smooth Tungsten	1960
Photonic Crystal	2740
Emission ratio PC/W	1.40

The proposed geometry can be scaled to different wavelengths of interest, including the infrared, where it will produce a tunable enhanced emission. Such uniquely narrow infrared emitters can have novel application to sensors where infrared absorbance of trace gases can be measured with higher sensitivity. Also, thermo-photovoltaic devices can heat up and recycle photons resulting in emission of photons in a narrow range that can very efficiently capture waste heat and convert solar thermal radiation.

Discussion and Conclusion

We demonstrate through the numerical simulation that the tungsten photonic crystal can have output light intensity 1.4 times as large as that of the smooth tungsten film under the same input power. Moreover the higher output light intensity of the tungsten photonic crystal than the smooth tungsten film implies that the tungsten photonic crystal filament may operate at lower temperature in order to have the same output light intensity, which would imply longer lifetime of the tungsten photonic crystal filament.

However there are certain serious experimental limitations of this tungsten photonic crystal. At high temperatures, above approximately 1600 ºC the periodic patterned surface structure of the tungsten can change severely [19]. The surface pattern in the tungsten photonic crystal can deform completely due to grain growth occurring in polycrystalline tungsten, roughening the surface and destroying the periodic pattern at the surface. Such roughening temperatures are far below the melting temperature of tungsten. The enhancement of the thermal emission will then not occur at high temperature. Further work is needed to explore potential ways to prevent the deformation of the tungsten photonic crystal at the high temperature necessary for incandescent emission.

References

1. T.W. Ebbesen, H.J. Lezec, H.F. Ghaemi, T. Thio, and P.A. Wolff, Nature (London) **391**, 667–669 (1998).
2. R. Biswas, C.G. Ding , I. Puscasu, M. Pralle, M. McNeal, J. Daly, A. Greenwald, E. Johnson, Phys. Rev. B. **74**, 045107 (2006).
3. David L. C. Chan, Marin Solja˘ci´c and J. D. Joannopoulos, Optics Express Vol. **14**, 8785 (2006).
4. CRC Handbook of chemistry and physics (2006). Page E-381.
5. I. Celanovic, D. Perreault, J. Kassakian, Phys. Rev. B.**72**, 075127 (2005)
6. I. Celanovic, F. O'Sullivan, M. Ilak, J. Kassakian, and D. Perreault, Opt. Lett. **29**, 863-865 (2004)
7. Z. Y. Li and L. L. Lin, Phys. Rev. E **67**, 046607 (2003).
8. H. G. Craighead, R. E. Howard and D. M. Tennant, Appl. Phys. Lett. **38**, 74 (1981).

9. H. Sai, H. Yugami, Appl. Phys. Lett., **85**, 3399 (2004)

10. H. Sai, Y. Kanamori, K. Hane, H. Yugami, M. Yamaguchi, Proceedings of the Thirty-first IEEE Photovoltaic Specialists Conference, 2005. page 762 (2005). Conference Record

11. H. Sai, H. Yugami, Y. Kanamori, J. Micromech. Microeng. **15**, 5243 (2005)

12. H. Sai, Y. Kanamori and H. Yugami, Appl. Phys. Lett., **82**, 1685 (2003).

13. Robert Siegel and John R. Howell, *Thermal Radiation Heat Transfer-4th ed*. (Taylor&Francis, New York, 2002)

14. Lawrence D. Woolf, Seeing the Light: The Physics and Materials Science of the Incandescent Light Bulb, Research Report General Atomics, February 20, 2002.

15. Stockman, A., & Sharpe, L. T. (2000). Vision Research, **40**, 1711-1737.

16. H. A. Jones, Phys. Rev. **28**, 202 (1926)

17. Sharpe, L. T., Stockman, A., Jagla, W. & Jägle, H.(2005). Journal of Vision, **5**, 948-968.

18. In the numerical simulation, absorption of smooth tungsten is calculated with 0.01μm step size, while for photonic crystal, due to computation load, it is obtained through interpolation from data with 0.05μm step size.

19. R. Biswas, S. Neginhal, C. G. Ding, I. Puscasu, E. Johnson, J. Opt. Soc. of America B **24**, 2489-95 (2007).

20. H. Sai, MRS Spring 2009 talk and unpublished. Similar roughening of tungsten surfaces has been observed in Ames Laboratory.

CHAPTER 4 MICROSTRIP PATCHES

Introduction

The objective of the simulation is to find out the optimal parameters for the microstrip patches to get strong absorption near the 10μm band using the design of a recently published paper [1]. Instead of the hole arrays used in previous simulation, we use the arrays of microstrip patches [Fig. 1] in the simulation.

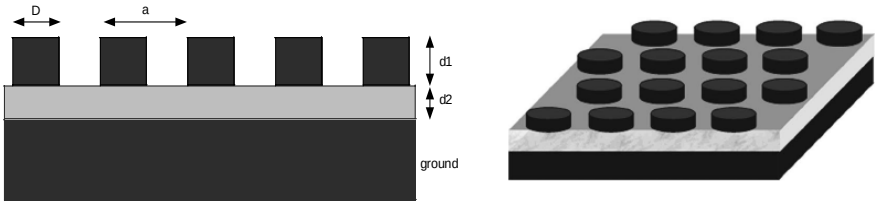

Figure 4.1 The triangular array of circular patches, with diameter D, height d_1 and period *a*, sits on a dielectric film of thickness d_2, which in turn covers a ground plane.

In our simulation, both the circular patches and ground plane are metal (Au). The dielectric film is Si_3N_4 with dielectric constant of 4.0. The ground plane (thickness d4) is much thicker than the skip depth of Au (~25nm at IR wavelengths). Such thick ground plane will lead to nearly zero transmission in the IR range. The period (a) is chosen to be 4.5μm in order to obtain primary resonance near 10μm.

Simulation Results

The absorption spectrum has a primary broad peak near 10μm and weak peaks at lower wavelengths. When d1 and d2 are both 0.1μm, the primary resonance (A~0.55) is at 10.6μm. The primary resonance is considered to arise from a localized surface plasmon,

which in turn is due to a standing wave of plasmons trapped below a metal patch [1]. The primary resonance of a circular patch occurs at

$$\lambda = \frac{\pi D}{1.841} n_d (1 + \frac{2c}{w_p d_2})^{1/2} \tag{4.1}$$

n_d (2.0) is the refractive index of the dielectric layer, w_p (2175 THz) is the plasmon frequency of Au in its Drude model. From (1), when d_2 is 0.1μm, the primary resonance is at 14.9μm and when d_2 is 0.2μm, the primary resonance at 11.84μm. There is also a weak sub-peak at ~9.0μm, which is believed to arise from the surface plasmon at the Au-dielectric interface. The wavelength of the sub-peak is consistent with the theory, which is $n_d \times a$=9.0μm.

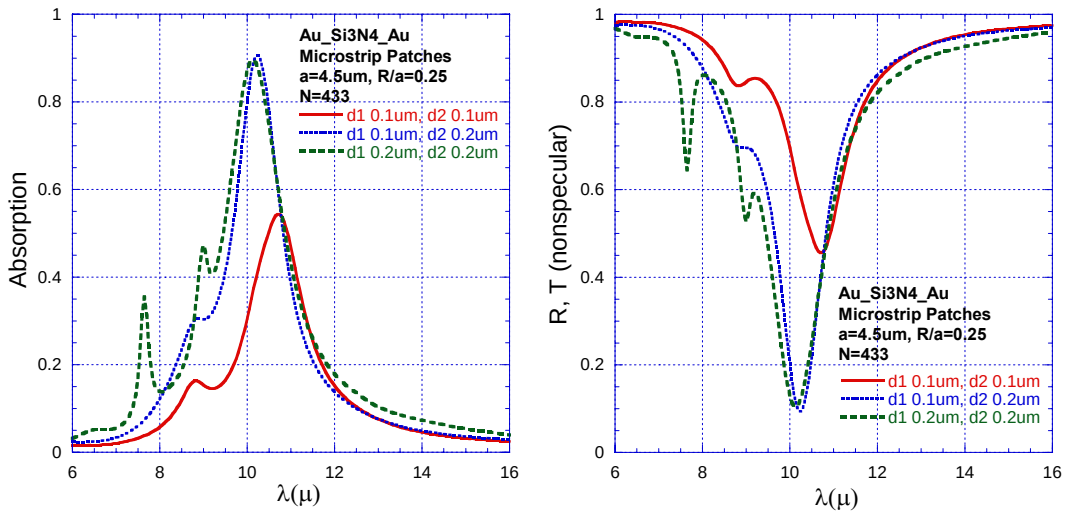

Figure 4.2. (a) Calculated absorption of the microstrip patch structure (b) Calculated nonspecular reflection of the microstrip patch structure.

When d_2 is increased from 0.1μm to 0.2μm and d_1 stays as 0.1μm, the magnitude of the primary resonance at 10.6μm increases to ~0.9. The wavelength of the primary resonance is shifted slightly to lower wavelength, ~10.2μm. Thus, the primary resonance is dependent on the thickness of the dielectric layer d_2. There is still a weak sub-peak at ~9.0μm.

To find the effect of the d_1 on the absorption, d_2 is kept at 0.2μm and d1 is increased from 0.1μm to 0.2μm. The wavelength of the primary resonance peak does not change, but the sub-peak at ~9.0 μm becomes sharper and a new sharp sub-peak appears at ~7.6μm. It is not clear yet why the new sub-peak at 7.6μm appears. The surface plasmon at the interface of Au and dielectric is strongly dependent on the d_1.

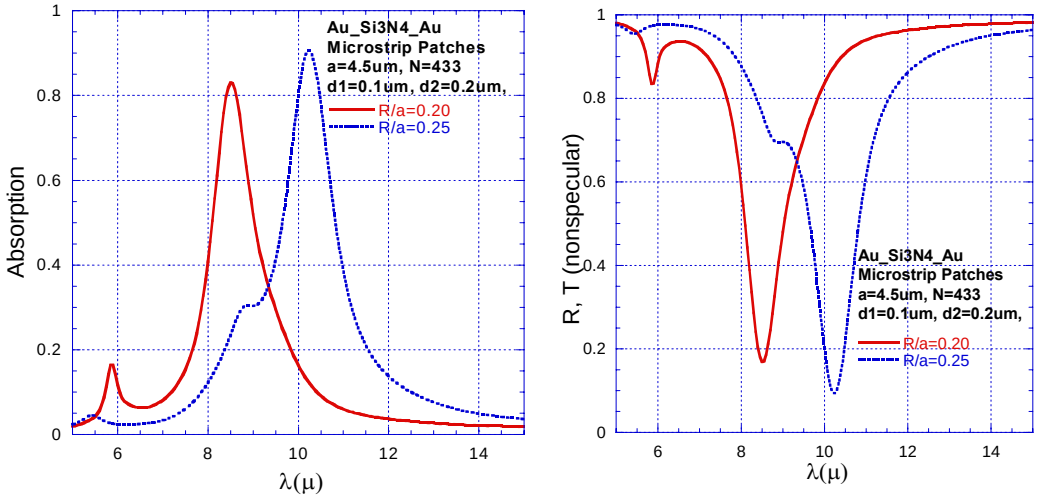

Figure 4.3. Absorption of microstrip patches for different circular patch diameters. (b) Nonspecular reflection of microstrip patches for different circular patch diameters

We next simulate the arrays of microstrip patches with different circular patch diameters. The d_1 is 0.1μm and d_2 0.2μm. As predicted by equation 1, when D is decreased,

the wavelength of the primary resonance will also decrease [Fig. 3]. At the same time, the magnitude of the primary resonance also becomes smaller and the primary absorption peak becomes narrower when the diameter of the circular patches decreases.

We also notice that there is a sharp peak near 4μm in the absorption spectrum [Fig. 4]. The absorption peak is very strong, e.g. A~0.9 when d_1 and d_2 are both 0.1μm. It's possible that the sharp absorption peaks near 4μm are from the higher order modes trapped below circular patches or due to the strong diffraction effects happening at wavelengths below the wavelength equal to the array period (4.5μm) [1].

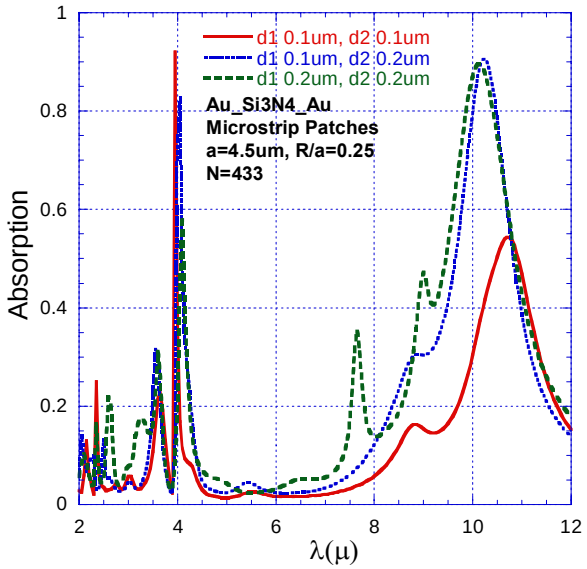

Figure 4.4. Calculated absorption of the microstrip patch structure including absorption at lower wavelengths.

In summary, a primary broad absorption (A~0.9) could be generated near 10 μm by designing the arrays of microstrip patches properly. The wavelength of the primary resonance is determined by the period of the array. The magnitude of the primary resonance is strongly dependent on the thickness of the dielectric layer. The metal-dielectric-metal layer

may act as a metamaterial in some aspects. The thickness of the circular patches almost does not affect the primary resonance. Smaller diameter of the circular patches will decrease the magnitude of the primary resonance and make the primary resonance narrower.

References

1. I. Puscasu and W. L. Schaich, “Narrow-band, tunable infrared emission from arrays of microstrip patches”, App. Phys. Lett., **92**, 233102 (2008)

ACKNOWLEDGMENTS

I would like to take this opportunity to express my thanks to those who helped me with various aspects of conducting research and the writing of this thesis.

First of all, I would like to thank my major professor, Dr. Rana Biswas, for his continuous support throughout this research and the writing of this thesis. I would also like to thank my committee members: Dr. Jiming Song, Dr. Jaeyoun Kim. Here, I thank you for your invaluable help, instruction and patience during the development of my research work.

I also would like to thank D. Zhou, L. Garcia and many other friends and colleagues for their help during the writing of this thesis.

I sincerely thank my parents who are always on my side and encouraging me through my life. My special thanks also go to my elder brothers and sisters for their love and support during my growth.